

# UC Irvine

## UC Irvine Electronic Theses and Dissertations

### Title

Constructing Low-Energy Effective Models for Real Materials

### Permalink

<https://escholarship.org/uc/item/5z60n2hv>

### Author

Sawaya, Randy Chafic

### Publication Date

2021

Peer reviewed|Thesis/dissertation

UNIVERSITY OF CALIFORNIA,  
IRVINE

Constructing Low-Energy Effective Models for Real Materials

DISSERTATION

submitted in partial satisfaction of the requirements  
for the degree of

DOCTOR OF PHILOSOPHY

in Chemical and Material Physics

by

Randy C. Sawaya

Dissertation Committee:  
Professor Steven R. White, Chair  
Professor Alexander(Sasha) Chernyshev  
Professor Ruqian Wu

2021



# DEDICATION

To my parents, Ramzy and Nancy Sawaya.

# TABLE OF CONTENTS

	Page
<b>LIST OF FIGURES</b>	<b>v</b>
<b>LIST OF TABLES</b>	<b>viii</b>
<b>ACKNOWLEDGMENTS</b>	<b>ix</b>
<b>VITA</b>	<b>x</b>
<b>ABSTRACT OF THE DISSERTATION</b>	<b>xiii</b>
<b>1 Introduction</b>	<b>1</b>
1.1 Three-Stage Downfolding using DFT . . . . .	4
1.1.1 Using Density Functional Theory to define $L$ and $H$ . . . . .	6
1.1.2 Wannier Functions . . . . .	7
1.1.3 Self-Energy and Screened Interaction . . . . .	10
1.1.4 Applications to Bulk Materials . . . . .	11
1.2 Downfolding with Similarity Transformations . . . . .	12
1.2.1 Löwdin Downfolding . . . . .	13
1.2.2 Canonical Transformations . . . . .	15
1.3 Fitting Reduced Hamiltonians to Accurate Simulations . . . . .	17
1.3.1 Density Matrix Downfolding . . . . .	18
<b>2 DMRG Methods for Electronic Structure</b>	<b>22</b>
2.1 Sliced-Basis DMRG . . . . .	23
2.1.1 Constructing the Sliced-Basis Functions . . . . .	24
2.1.2 Compressing the Long-Range Interactions . . . . .	28
2.2 sb-DMRG on Hydrogen Chains . . . . .	30
2.2.1 Initializing sb-DMRG with Hartree-Fock . . . . .	30
2.2.2 Reducing to Slice Natural Orbitals . . . . .	31
2.2.3 Boundary Conditions . . . . .	33
<b>3 The Hydrogen Chain</b>	<b>34</b>
3.1 Ground State Properties . . . . .	35
3.1.1 Nature of Metal-Insulator Transition . . . . .	37

<b>4</b>	<b>Deriving Effective Models for the Hydrogen Chain</b>	<b>43</b>
4.1	Simulating the Hydrogen Chain . . . . .	44
4.2	Wannier Functions for Interacting Systems . . . . .	45
4.3	Variational Optimization of Effective Models . . . . .	50
4.3.1	From Long-Range Interactions to On-site $U$ . . . . .	54
4.4	H-Chain Effective Models . . . . .	57
4.4.1	Truncating the Four-Index Interactions . . . . .	58
4.4.2	Long-Range Effective Models . . . . .	59
4.4.3	Reducing the Range of the Interactions . . . . .	61
4.4.4	Hubbard Model for the H-chain . . . . .	64
<b>5</b>	<b>Conclusion</b>	<b>67</b>
	<b>Bibliography</b>	<b>69</b>
	<b>Appendix A Appendix</b>	<b>75</b>

# LIST OF FIGURES

	Page	
1.1	The general recipe followed by the three-stage downfolding procedure. The images used to create this figure are taken from [26]. . . . .	5
2.1	A schematic representation of the sliced-basis functions for systems arranged in a 1D chain geometry. The atoms are represented by the small blue circles with atomic spacing $R$ . On the left, the grid points along the chain are shown which when zoomed in shows a cartoon of the slices separated by a distance $a$ . On the right, the usual spherically-symmetric Gaussian basis functions are generalized to cylindrical symmetry which the sliced-basis is designed to capture. . . . .	23
2.2	Ground state electron density for H10 at $R = 1.0a_B$ . The regions filled in with red represent the end spill-off of the electron density due to the large empty regions on either side of the chain. . . . .	33
3.1	Ground state electron structure and magnetic phases of the H-chain. (a) sb-DMRG calculation with 11 basis functions for H12 at $R = 1.8a_B$ . There is a very apparent dimerization of the electrons. (b). Magnetic phases from DFT-PBE taken from [48]. Here $M_{\text{tot}} = \int d^3r m(r)/N$ and $M_{\text{abs}} = \int d^3r  m(r) /N$ where $m(r)$ is the magnetization of the simulation cell. . . . .	35
3.2	Ground state properties of the H-chain. (a) The anti-ferromagnetic correlations in H60 for $R = 2.0a_B$ and $R = 3.2a_B$ . The inset shows a power law decaying envelope for the correlations. (b) The dimerization in various lattice models as compared with the H-chain. For the Hubbard model, the dimerization is defined as $\Delta_{\text{dim}} = \left  \left( \hat{c}_{N/2}^\dagger \hat{c}_{N/2+1} + h.c. \right) - \left( \hat{c}_{N/2+1}^\dagger \hat{c}_{N/2+2} + h.c. \right) \right $ . For the Heisenberg model, it is defined as $\Delta_{\text{dim}} = \left  \hat{S}_{N/2} \hat{S}_{N/2+1} - \hat{S}_{N/2+1} \hat{S}_{N/2+2} \right $ . And for the H-chain, it is defined as the difference in the density between two adjacent bonds connecting the $N/2$ and $N/2 + 1$ hydrogen atoms. . . . .	36
3.3	Natural orbital occupancy calculated by diagonalizing the single-body correlation matrix for H10 at (a) $R = 0.9a_B$ and (b) $R = 3.3a_B$ . For small $R$ , the system is metallic and shows non-zero occupancy in the diffuse $p$ orbitals. On the opposite end, in the insulating phases, the occupancy is primarily dominated by compact $s$ -type character. . . . .	37

3.4	Ground state entanglement and density. (a) The von Neumann entanglement measured along the 1D chain for H10 at different values of atomic spacing. As $R$ increases, the dimerization persists, but weakens. This is also seen by comparing the density and even and odd bonds as shown in the left column for (b) $R = 1.4a_B$ and (c) $R = 3.6a_B$ . In all plots, the dashed lines correspond to the positions of the nuclei. . . . .	38
3.5	Gaussian basis that are used to make the sliced-basis functions. The $s$ -type function labeled by “Contracted” is a contraction of the $\zeta = 1.962$ and $\zeta = 13.01$ Gaussians with coefficients 0.1379770 and 0.0196850, respectively. For the $p$ -type functions, only the $p_x$ are shown. The $p_y$ functions are the same except they extend the $y$ -axis instead of the $x$ -axis. . . . .	39
3.6	Natural Orbitals and their corresponding occupancies for the $s$ - and $p$ -blocks of the one-body correlation matrix. (a) As $R$ is increased, we can see the extra electron moving from the $2p$ NO to the $2s$ NO. These orbitals are shown in (b) and (c). Note that the $x$ - $y$ symmetry is broken here and the extra electron arbitrarily chooses to occupy $2p_x$ . The symmetry is expected to be restored when the number of states kept tends to infinity. . . . .	40
3.7	Energy differences in occupying $2s$ versus $2p$ . (a) The energies for the two states given in (3.3) and (3.4) as a function of $R$ . The pie charts above each point indicate the $2s$ and $2p$ occupancy of the extra electron in the original system. The density relative to half-filling of the doped system is shown in (b) when the extra electron mostly occupies the $2p$ NO and in (c), when it mostly occupies the $2s$ NO. . . . .	41
4.1	Eigenvalues of the single-particle correlation matrix from the ground state of H20 giving the natural orbital occupancy. The first 10 states are doubly occupied and represent Hartree-Fock type states. The second 10 states have small but non-negligible occupancy. States beyond the first 20 show occupancy on the order of $10^{-3}$ and are truncated to give a downfolding approximation. . . . .	45
4.2	Translationally invariant Wannier function for (a) $R = 2.0a_B$ and (b) $R = 3.2a_B$ constructed from the single-particle density matrices of H100. The top panels in each subplot show the full 3D Wannier functions in real-space integrated over $y$ and the lower panels, the 1D representation within the sliced basis as a function of $z$ for both sb-DMRG and Hartree-Fock derived functions. . . . .	48
4.3	Hamiltonian parameters from transforming the H-chain Hamiltonian into an effective model using the Wannier functions for H100. All parameters are scaled by the average value of the nearest neighbor hopping denoted by $\bar{t}$ . The top panel shows the single-body terms and the lower panel, the two-body interaction terms. The dashed lines in the lower panel are $1/r$ lines in units of $\bar{t}$ . . . . .	49



4.4	Comparison of the variational algorithm and a brute force search. The solid red and blue curves give the value of the ground state overlap between the long-range model(with $U = 2.0$ in blue and $U = 7.4$ in red) and the Hubbard model evaluated on a fine grid. The various vertical lines show the values of $U_{\text{eff}}$ that correspond to the naive effective model with $U_{\text{eff}} = U/2$ , the model found varationally and the best possible model. . . . .	55
4.5	Spin velocities for the H-chain and two effective models defined in (4.12) and (4.15). The top row shows (a) 2-spinon and (b) 4-spinon excitation gaps at $R = 2.0a_B$ for the H-chain, its corresponding directly transformed model denoted as $\hat{H}_{\text{WF}}$ and optimal Hubbard model, $\hat{H}_{\text{Hub}}$ . The same is done at $R = 3.2a_B$ in the lower row for the (c) 2-spinon and (d) 4-spinon excitations. The numbers in the legend correspond to the slope of the fitted lines which give the spin velocities. . . . .	60
4.6	Single-particle correlations for the H-chain, its corresponding directly transformed model defined in (4.12) and optimal Hubbard model defined in (4.15) for H100 at (a) $R = 2.0a_B$ and (b) $R = 3.2a_B$ . The correlators are calculated from the middle of the chain to the right edge as defined in (4.13). Note here that, the WFs are used to transform the H-chain correlation functions into the same space as the effective models. . . . .	61
4.7	Spin-spin correlations at (a) $R = 2.0a_B$ and (b) $R = 3.2a_B$ for the original H-chain and its corresponding effective models defined in (4.12) and (4.15). The correlators are calculated from the left-most edge of the chain to the midpoint for a system of 100 atoms. The H-chain correlations have been scaled such that the point at site 50 match that of $\hat{H}_{\text{WF}}$ . . . . .	62
4.8	(a) Error for effective models with varying-range one-body and two-body interactions for H20 at $R = 2.0a_B$ . The dashed black lines correspond to the error made by using only Hubbard interactions in the effective model as in (4.15). Increasing the range of the two-body interactions is seen to be more effective than increasing the range of the one-body hopping. (b) Decay of two-body interactions with varying maximum range for H40. The variable $l_V$ is defined as the maximum range of the two-body interactions. For example, $l_V = 1$ implies a range up to nearest-neighbor, $l_V = 2$ , next nearest-neighbor, etc. The dashed black line shows the decay of the two-body interactions for $\hat{H}_{\text{WF}}$ scaled by the average nearest-neighbor hopping. The other lines are the two-body interactions for the corresponding effective model with only a nearest-neighbor hopping term and a limited range two-body interaction. The error as defined in (4.14) is also shown in the last column of the legend. . . .	63
4.9	Optimal Hubbard parameters for each H-chain as a function of the atomic spacing, $R$ for H100. The resulting Hubbard model becomes “strongly correlated” near $R = 3 - 4a_B$ where the corresponding value of $U/t$ becomes larger than the bandwidth of about $4t$ . The dashed red line shows the optimization error as defined in Eq. (4.14). . . . .	65

# LIST OF TABLES

	Page
4.1 CC-pVDZ Basis Set. The contracted basis function shows the coefficient with the corresponding Gaussian width in parentheses. . . . .	44

# ACKNOWLEDGMENTS

RCS was supported by the Simons Foundation through the Many Electron collaboration.

I would first and foremost like to thank my advisor Steve White for his years of guidance and patience, not just for his physical insight but also for his well received advice in writing and presenting information. I would also like to thank my group mates, Mingru Yang, Shengtao Jiang, Yifan Tian and Yiheng Qiu for the all useful discussions, group lunches and get-togethers. Our discussions always made me excited about relevant research and new ideas.

For pushing me to go to graduate school in the first place, I would like to thank Ziad Haddad. He was with me every step of the way and I learned a lot from him in regards to research as well as how to go through graduate school and life in general. He opened many doors for me and always gave me every opportunity to do my best work.

And finally, I wouldn't be where I am today if it wasn't for my parents, Ramzy and Nancy Sawaya. I am very grateful for all the years of guidance and encouragement and look forward to the many more years of learning from them; they were my first teachers. I would also like to thank my sisters Melissa and Jessie Sawaya for always being there, and not just to play Halo. And lastly, I would like to thank all my close friends who put up with my antics over the years. To Jeremy Beckman, Howard Cheung, Cassidy Feltenberger, Lauren Fitzgerald, Josh Friedberg, José Gaun-Zhou, Khalil Gobir, Alex Goodwin, Andrew Gunawan, Brandon Huynh, Arian Kangarani, Scott Kelly, Brendan Ma, Stacie Overmeyer, Zubair Serang, and Ashleigh Wong.

# VITA

Randy C. Sawaya

## EDUCATION

<b>Doctor of Philosophy in Chemical and Materials Physics</b> University of California, Irvine	<b>2021</b> <i>Irvine, California</i>
<b>Bachelor of Science in Physics</b> University of California, Irvine	<b>2016</b> <i>Irvine, California</i>
<b>Bachelor of Science in Aerospace Engineering</b> University of California, Irvine	<b>2016</b> <i>Irvine, California</i>

## RESEARCH EXPERIENCE

<b>Graduate Research Assistant</b> University of California, Irvine	<b>2016–2021</b> <i>Irvine, California</i>
<b>Graduate Student Intern</b> Primer Technologies	<b>June 2021–August 2021</b> <i>San Francisco, California</i>
<b>Student Researcher</b> Jet Propulsion Laboratory, California Institute of Technology	<b>2015–current</b> <i>Pasadena, California</i>

## TEACHING EXPERIENCE

<b>Teaching Assistant</b> University of California, Irvine	<b>2016–2018</b> <i>Irvine, California</i>
<b>Learning &amp; Academic Resource Center Tutor</b> University of California, Irvine	<b>2014–2016</b> <i>Irvine, California</i>

## REFEREED JOURNAL PUBLICATIONS

- Constructing Hubbard Models for the Hydrogen Chain using Sliced Basis DMRG** in review  
Physical Review B
- Assimilation of DAWN Doppler wind lidar data during the 2017 Convective Processes Experiment (CPEX): impact on precipitation and flow structure** 2021  
Atmospheric Measurement Techniques
- Ground-State Properties of the Hydrogen Chain: Dimerization, Insulator-to-Metal Transition, and Magnetic Phases** 2020  
Physical Review X
- Interpreting millimeter-wave radiances over convective clouds** 2017  
Journal of Geophysical Research: Atmospheres

## REFEREED CONFERENCE PUBLICATIONS

- Estimating Vertical Mass Flux in Convective Storms from Low-Earth-Orbit Convoys of Miniaturized Microwave Instruments** Dec 2021  
AGU Fall Meeting 2021
- Geophysical descriptors of the vertical structure of convective storms retrieved from satellite passive microwave observations with different a-priori constraints** Dec 2021  
AGU Fall Meeting 2021
- Passive Microwave Split-Step Retrievals of the Vertical Structure of Condensed Water and Water Vapor in Deep Convective Clouds** Jan 2020  
AMS Annual Meeting 2020
- Phase Transitions and Magnetic Ordering in the 1D Hubbard Chain** Jun 2018  
APS March Meeting 2018

## **SOFTWARE**

**HChain2EffModel**                    <https://github.com/rcsawaya/HChain2EffModel.git>  
*Codes to derive effective models for the H-chain.*

# ABSTRACT OF THE DISSERTATION

Constructing Low-Energy Effective Models for Real Materials

By

Randy C. Sawaya

Doctor of Philosophy in Chemical and Material Physics

University of California, Irvine, 2021

Professor Steven R. White, Chair

Sliced-basis DMRG(sb-DMRG) is used to simulate a chain of hydrogen atoms and to construct low-energy effective Hubbard-like models. The downfolding procedure first involves a change of basis to a set of atom-centered Wannier functions constructed from the natural orbitals of the exact DMRG one-particle density matrix. The Wannier function model is then reduced to a fewer-parameter Hubbard-like model, whose parameters are determined by minimizing the expectation value of the Wannier Hamiltonian in the ground state of the Hubbard Hamiltonian. This indirect variational procedure not only yields compact and simple models for the hydrogen chain, but also allows us to explore the importance of constraints in the effective Hamiltonian, such as the restricting the range of the single-particle hopping and two-particle interactions, and to assess the reliability of more conventional downfolding. The entanglement entropy for a model's ground state, cut in the middle, is an important property determining the ability of DMRG and tensor networks to simulate the model, and we study its variation with the range of the interactions. Counterintuitively, we find that shorter ranged interactions often have larger entanglement.

# Chapter 1

## Introduction

Understanding the electronic properties of complex systems such as transition metal oxides, organic compounds and high- $T_c$  superconductors has emerged as a central theme in condensed matter physics which has spurred a large effort to extend the applicability of existing theoretical tool-kits to these exotic materials. One of the most well known and widely applied techniques in tackling realistic materials has been Density Functional Theory(DFT).[24, 32] In it's early days, the Local Density Approximation(LDA)[32] led to many successful calculations for row-one atoms and dimers as well as polymers and other extended systems of alkali and alkaline metals.[29] However, it quickly became apparent that the approximations in LDA could not be successfully applied to more strongly correlated materials and in some cases can predict metallic behavior for Mott insulating systems such as in the copper oxide superconductor,  $\text{La}_2\text{CuO}_4$ [45, 25]. Since LDA, many more complicated functionals have been proposed, including B3LYP[68, 35, 5, 62] and the well-known Perdew-Burke-Ernzerhof(PBE) functional[54] which significantly improved on LDA, but still have trouble with some strongly-correlated systems. This has led to a more restricted use of DFT, namely as a first step in deriving an effective model which later will be solved by a method that can more accurately treat strong correlations such as the Density Matrix Renormalization



Group(DMRG), Quantum Monte Carlo(QMC) or Dynamical Mean-Field Theory(DMFT). This approach has been dubbed “downfolding” and has become a mainstream technique for calculating properties of realistic materials that are otherwise too difficult to simulate directly.

In conventional downfolding applications, the accuracy of resulting effective models are verified by comparing to experimental results. However, one thing that has been notably missing is the ability to use an accurate and reliable strongly correlated method directly on the full system in order to check the many approximations that accompany the downfolding process. For instance, a central approximation to these techniques in the constrained Random Phase Approximation(cRPA) which has only recently been tested in the context of mapping multiorbital Hubbard models to their low energy representations.[58] The main difficulty in these direct validations lies in the lack of availability of sufficient algorithms that can simulate realistic systems. Recently, however, there has been a large effort to push methods which have been traditionally used for strongly correlated model Hamiltonians to the realm of more realistic materials. Investigating the simplest systems of these complex materials, the Hydrogen chain(H-chain) emerged as a natural starting point for improving current state of the art many-body methods and has been the focus of several studies.[47, 48]

Focusing on the H-chain, in this work we develop a downfolding approach to derive effective low-energy models each with a varying set of one- and two-body terms that have been determined variationally using a variant of DMRG known as sliced-basis DMRG. Very broadly, “downfolding” may refer to any technique that is used to arrive at some effective low-energy representation of a much more complicated many-body system.[26] For any successful downfolding procedure, the resulting model should accurately describe the relevant physics of the original system, while maintaining enough simplicity to efficiently simulate the model in a regime that gradually approaches the thermodynamic limit. In this way, the finite size effects, long-range order, phases, etc. of the original system may be studied without the need

for directly simulating it at larger and larger system sizes.

Early effective theories such as Band theory and Fermi liquid theory were successful at describing a subset of these systems, but it wasn't soon after that systems with much stronger electron correlations such as high- $T_c$  superconductors, transition-metal oxides and rare-earths became the main focus. This led to development of many effective models such as the Hubbard,  $t$ - $J$  and Anderson Impurity model, each derived with the intention of accurately describing some relevant aspect of strongly-correlated materials(e.g. the behavior of  $d$  and  $f$  shell electrons for the Hubbard model). The key question then becomes, how does one arrive at the correct model parameters to properly describe a specific material? One can take a semi-empirical approach and use data from experiments to estimate the couplings for each of the terms in the effective model.[7, 6, 8, 9] Or, on the other hand, one can attempt an *ab initio* calculation that can not only determine the model parameters, but also the model that best describes the system of interest.[21, 20, 2, 1, 61, 60] In either case, downfolding aims to map the full Hilbert space of the original system into a much simpler subspace that acts on a selected few degrees of freedom.

This chapter focuses on the *ab initio* downfolding techniques, which can lead to a more physical explanation for using a particular model and offer insight into how one can construct a general procedure for deriving effective models. Here we explore several techniques that are most frequently employed to describe systems ranging from single-atoms and small molecules to bulk materials. First in section 1.1, we discuss the most commonly used technique employed in downfolding: a three-stage approach using DFT inspired by the same ideas used in the Wilson Renormalization Group. Then in section 1.2, we investigate a different approach based on similarity transformations of the original Hamiltonian. Finally in section 1.3, we discuss a recent method based on matching one and two-body density matrices between the original and effective systems.

Then in chapter 2, we give an introduction to the sliced-basis formalism and it's application

to the H-chain. In chapter 3 we review some results on the ground state properties of the H-chain as well as give new results on the nature of the metal-to-insulator transition. The main procedure used to derive different effective models is then presented in chapter 4 followed by the conclusion and summary of contributing results in chapter 5.

## 1.1 Three-Stage Downfolding using DFT

At the heart of any Downfolding method is the renormalization group notion of partitioning the full Hilbert space into high and low-energy subspaces and integrating out the high energy degrees of freedom. In general, the two spaces will be coupled and we can represent the total action as the sum of these three pieces

$$S = S_L + S_H + S_{LH} \tag{1.1}$$

where the subscripts  $L$  and  $H$  denote the low and high-energy subspaces, respectively. The coupling between these spaces is represented by  $S_{LH}$ . The process of integrating out the high energy subspace involves tracing out those degrees of freedom. The partition function is then rewritten in terms of only the low energy variables:

$$\begin{aligned} Z &= \text{Tr}[e^S] \\ &= \text{Tr}_L[\text{Tr}_H[e^S]] \\ &= \text{Tr}_L[e^{S'}] \end{aligned} \tag{1.2}$$

where  $S' = \log \text{Tr}_H[e^S]$  defines the effective, low-energy action, giving us our downfolded model. What remains is to specify how to trace over the high-energy degrees of freedom, say by a perturbative treatment, which then introduces an approximation. More accurate treatments are also possible, as Wilson showed with his numerical renormalization group. In

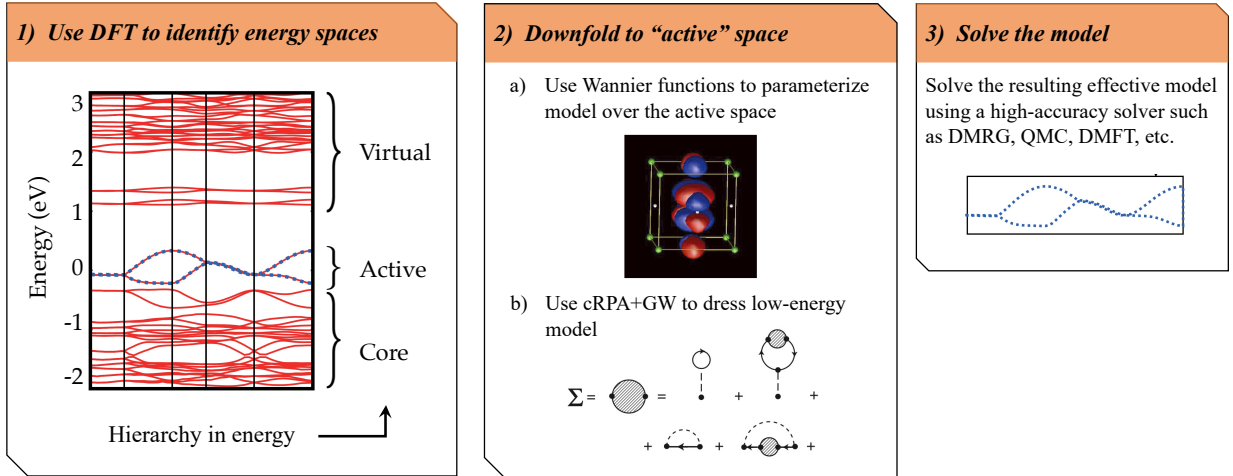


Figure 1.1: The general recipe followed by the three-stage downfolding procedure. The images used to create this figure are taken from [26].

this thesis, we discuss methods based on the density matrix renormalization group, a more modern and improved version of Wilson’s method.

Before applying any such procedures, the  $L$  and  $H$  subspaces need to be properly defined. A good choice is crucial for approximate methods, such as perturbation theory, and still essential for nonperturbative approaches which still may fail. In many strongly correlated materials, there exists a natural separation of low and high energy spaces based on their proximity to the Fermi level.[28, 27, 50] In regions far away, states are either fully occupied or empty, leading to weak correlations. But in a small energy window around the Fermi level, strong correlations arise due to the poor mutual screening of the electrons caused by a small number of isolated bands. As we will see in the next section, this hierarchy of energies emerges naturally from the Local Density Approximation in Density Functional Theory, which will ultimately provide us with a general method for identifying  $L$  and  $H$ .

Defining these spaces is the first step in the three-step downfolding approach summarized in Fig. 1.1 and discussed in the next section. After separating the target space from the rest, Wannier functions(see section 1.1.2) are typically used to parameterize an effective model defined over the low-energy degrees of freedom. At this stage, the model needs to be dressed

by the high-energy contributions to include correlation effects which is typically done via the constrained Random Phase Approximation(cRPA) within GW(see section 1.1.3). The result is an effective model representing the original system defined exclusively over the low-energy space which now needs to be solved using a high-accuracy solver such as DMRG, QMC, DMFT, etc.

### 1.1.1 Using Density Functional Theory to define $L$ and $H$

One of the early successes in tackling the many-electron problem was the development of Density Functional Theory(DFT)[24, 32, 29], which allows the many-body nature of the original problem to be reformulated in terms of a functional on the electron density. It was inspired by an observation of Hohenberg and Kohn which first noticed that any many-electron system under the influence of an external potential can be uniquely described by the electron density. This statement was formalized under the Hohenberg-Kohn (HK) theorems[24], which was first derived in the case of non-degenerate ground states, but later extended by Levy to the degenerate case[37].

The energy functional used in DFT gives the exact description of the many-body system, but its true form is unknown. The challenge, therefore, lies in developing practical approximations to the energy functional in order to accurately represent the system in a computationally tractable manner. The most widely used of these approximations is the Local Density Approximation(LDA) proposed by Kohn and Sham[32] which maps the energy functional into a non-interacting, single-particle Hamiltonian described by a set of single-particle states. This auxiliary system comes equipped with an effective single-particle potential whose functional form is typically determined by perturbation theory, the Random Phase Approximation(RPA) or Quantum Monte Carlo calculations of a uniform electron gas. As such, LDA is expected to accurately represent systems in which the electrons are spatially

homogeneous or weakly correlated, but breaks down for more strongly correlated systems.

When the size of the effective interaction approaches or exceeds that of the bandwidth, the band structure may be completely reconstructed throughout the entire Brillouin Zone, which correspond to local spatial reconstructions that invalidate the homogeneity of LDA. Therefore in the presence of strong interactions, states within an energy window around the Fermi level may not be captured well under LDA, while those far away can. The ability for LDA to adapt to this non-locality may be significantly improved by incorporating local gradient information as is done with the most well-known of these functionals, PBE[54]. Although these newer functionals vastly improve upon LDA, some strongly-correlated systems remain difficult to capture properly due to the fluctuations around an energy window near the Fermi level. This provides a natural separation of “high” and “low” energy spaces which underlines the main ideas behind downfolding.

In this context, the procedure then is to first run a DFT calculation on the original system which yields the band structure and then identify a small set of isolated bands near the Fermi level which will define the “target space” of the subsequent low energy model. Once these regions are identified, the Hamiltonian can be projected into the target space and renormalized to include the effects of higher energy states which will yield the final effective model.

### **1.1.2 Wannier Functions**

While there are many different ways of obtaining a model Hamiltonian defined over the target space(see the remaining sections of this chapter), one common approach is to use Wannier functions(WFs)[69, 31, 15] to project the original Hamiltonian into its corresponding model space. In the independent-electron picture, WFs are defined as linear combinations of Bloch orbitals, which are eigenstates of a one-body Hamiltonian. The one-body Hamiltonian is

the result of a specific approximation, such as a tight-binding model or, in this case, a density functional calculation. Even within these approximate theories, where the electronic ground state is fully specified by the single-particle states, the inherent  $U(1)$  symmetry of the Bloch orbitals grants the resulting WFs a type of “gauge freedom”, making them highly non-unique.

In the context of constructing model Hamiltonians, the choice of gauge determines the complexity of the interactions and, in principle, leads to an infinite family of models which are meant to describe the original system. It is important to note that the final results are independent of the chosen gauge, but, when building effective models, a judicious choice can lead to a much simpler Hamiltonian. This can be achieved by choosing the “Maximally localized” gauge of Marzari and Vanderbilt[44] which leads to a set of highly localized WFs, making the resulting model interactions short-ranged(see [43] for a nice review).

Let  $\{\psi_{n\mathbf{k}}\}$  be the set of eigenfunctions from a DFT calculation where  $n$  denotes the band index and  $\mathbf{k}$ , the crystal momentum. We assume here that the set  $\{\psi_{n\mathbf{k}}\}$  is chosen to represent a group of “low-energy” bands near the Fermi level which are separated by a finite gap from another set of “high-energy” bands(we briefly remark on the case in which there is no clear group of isolated bands at the end of the section). The Wannier function for the  $n^{th}$  band centered on the atom at position  $\mathbf{R}$  is defined as

$$w_{n\mathbf{R}}(\mathbf{r}) = \frac{V}{(2\pi)^3} \int d^3\mathbf{k} e^{-i\mathbf{k}\cdot\mathbf{R}} \psi_{n\mathbf{k}}(\mathbf{r}) \quad (1.3)$$

When considering only a single band, the eigenfunctions are defined up to a phase  $\tilde{\psi}_{\mathbf{k}}(\mathbf{r}) = e^{i\phi(\mathbf{k})} \psi_{\mathbf{k}}(\mathbf{r})$  which grants the WF its non-uniqueness. In the multi-band case, this  $U(1)$  symmetry generalizes to a  $U(N)$  symmetry, allowing each of the eigenfunctions to be defined up to a unitary transformation  $\tilde{\psi}_{n\mathbf{k}}(\mathbf{r}) = \sum_m \mathcal{U}_{nm}(\mathbf{k}) \psi_{m\mathbf{k}}(\mathbf{r})$ . The maximally localized

prescription then writes the WFs according to

$$\tilde{w}_{n\mathbf{R}}(\mathbf{r}) = \frac{V}{(2\pi)^3} \int d^3\mathbf{k} e^{-i\mathbf{k}\cdot\mathbf{R}} \tilde{\psi}_{n\mathbf{k}}(\mathbf{r}) \quad (1.4)$$

and fixes the gauge by optimizing the elements of  $\mathcal{U}$  such that

$$\Omega = \sum_n [\langle \tilde{w}_{n\mathbf{0}} | \mathbf{r}^2 | \tilde{w}_{n\mathbf{0}} \rangle - (\langle \tilde{w}_{n\mathbf{0}} | \mathbf{r} | \tilde{w}_{n\mathbf{0}} \rangle)^2] \quad (1.5)$$

is minimized. In general, the projected position operators shown in the expression for  $\Omega$  will not be simultaneously diagonalizable for  $x$ ,  $y$  and  $z$  meaning that the most optimal localization will only be approximately achieved. But for 1D systems, the 1D position operator (say  $x$ , for instance) can easily be projected into the WF basis and subsequently diagonalized to retrieve the coefficients which optimally localized the WFs according to (1.5). Once this is achieved, the Hamiltonian can be expressed as

$$H_{nm}(\mathbf{R}) = \langle \tilde{w}_{n\mathbf{0}} | H | \tilde{w}_{m\mathbf{R}} \rangle \quad (1.6)$$

So far, we have only discussed the case in which there is a finite gap that clearly defines a low and high-energy subspace. But for many applications, the energy window that is being targeted may have bands that continue beyond the window and hybridize with other, higher-energy bands, leaving some ambiguity in defining the target space. For example, when constructing effective Hamiltonians for complex systems, the bands that are to make up the model may be partially occupied in the energy window of interest. In these cases, we would like to have a set of  $N$  WFs which describe  $\mathcal{N}_k \geq N$  states at each point  $k$  in the Brillouin zone of the original system. This is done by first selecting a set of trial localized orbitals (e.g. spherical harmonics multiplied by Gaussians) and projecting these functions into the space spanned by the  $\mathcal{N}_k$  states.[16] The projected functions can then be orthonormalized using Löwdin orthogonalization[40], defining the functions  $\{\tilde{\psi}_{n\mathbf{k}}\}$  used in (1.4). In this case, the



gauge is specified by the choice of trial orbitals rather than the minimization criteria (1.5). However, given that the new set  $\{\tilde{\psi}_{n\mathbf{k}}\}$  forms an orthonormal basis, one may further localize them by taking linear combinations of the functions with coefficients found by minimizing (1.5), just as in the original formulation of maximally localized WFs.

### 1.1.3 Self-Energy and Screened Interaction

The results of the previous section give us a Hamiltonian defined over the low-energy space we are targeting, up to errors associated with the accuracy of the method used to derive the low-energy bands and subsequent WFs. For some semiconductors and insulators, the approximations employed by DFT tend to severely underestimate the band gap and in some cases can predict metallic behavior.[72, 63, 36] Given that the methods typically employed come with significant errors when applied to strongly correlated materials, we expect that the resulting Hamiltonian must be corrected in order to give a reliable description of the original system. These corrections can be calculated from many-body perturbation theory by expanding in the Coulomb interaction. As such, they are only approximate and depend on the type of system and the order out to which the corrections are calculated. The first-order correction gives Hartree-Fock which widens the gap, but over corrects and leads to a wider theoretical gap relative to experiments. The solution instead is to expand in the screened Coulomb interaction which forms the basis of the GW approximation.[23, 3]

The GW approximation gives self-energy and screened Coulomb interaction corrections to the one-body and two-body terms in the original Hamiltonian, respectively. In typical applications, the bare Green's function is corrected by higher-order terms that neglect vertex corrections leading to the Random Phase Approximation(RPA).[3]. But in the context of Downfolding where the original space has been separated *a priori* into high- and low-energy subspaces, only the low-energy degrees of freedom need to be renormalized by the effects

of the high-energy ones. Therefore, when computing corrections, only terms over this high-energy space are summed over leading to a version of RPA known as constrained RPA(cRPA). New one- and two-body terms are then defined within this approximation, giving a new effective Hamiltonian.

It is important to note that the accuracy of cRPA is most often not known or tested in many applications (this has been noticed by Shinaoka et al. which prompted a study concerning the accuracy of cRPA[58]) and is used as part of a larger recipe. Generally speaking, when the magnitude of the screened interaction is far smaller than the average energy scale determined by the bandwidth, cRPA can be a good approximation. But without carefully checking this condition, it is possible to erroneously apply the approximation.

#### 1.1.4 Applications to Bulk Materials

The techniques described in the previous sections outline a three-step Downfolding procedure that can be used in general to derive effective lattice models for real materials:

1. Use DFT to identify low- and high-energy states from the band structure. Then using this separation states, create a set of localized WFs for each band in the low-energy sector and project the original Hamiltonian into this space
2. Use GW to derive the self-energy and screened interaction corrections to the projected low-energy Hamiltonian in order to get a more accurate effective model
3. Use a low-energy solver such as QMC, DMFT, DMRG, etc. to calculate properties of the new model

This technique has been applied whenever there exists experimental data to compare against. For *sp* semiconductors and insulators, this has led to errors in the band gap of around

10-15% for moderately correlated materials, much lower than the traditional estimates by LDA alone.[67] For more strongly correlated materials, improvements on the original GW method led to a variant known as quasiparticle self-consistent GW which carries the success of the original method over to the strongly correlated regime.[67, 17, 33] In addition to semiconductors and insulators, transition-metal oxides such as SrVO<sub>3</sub>, VO<sub>2</sub>, Sr<sub>2</sub>VO<sub>4</sub> and YVO<sub>3</sub> have also been described by single-band and multi-band effective models.[38, 53, 10, 28, 27, 51, 14] Work has also focused on describing iron-based superconductors with modified Hubbard models.[46, 49, 4]

Historically, this has been the most prevalent method for deriving theoretical models from *ab initio* calculations. Additionally, there have been other techniques that focus on unitary transformations of the Hamiltonian itself which can be used to derive effective models. As we will see in the following section, these come with their own set of solutions and problems.

## 1.2 Downfolding with Similarity Transformations

In the previous section, we saw that the low-energy Hamiltonian must be corrected by expanding in a screened Coulomb interaction within the cRPA approximation in order to dress the low energy degrees of freedom with effects from the complimentary space. In addition to the methods already discussed, there exists another class of *ab initio* downfolding methods that provides an alternative approach to deriving effective models. These methods work directly with the Hamiltonian and attempt to find a similarity transformation that casts the original problem into its low-energy counterpart.

### 1.2.1 Löwdin Downfolding

The first of these methods is due to Per-Olov Löwdin and is often referred to as Löwdin partitioning or Löwdin Downfolding.[41, 42] This technique has been successfully applied to single atoms and small molecules[19, 65], but has yet to be implemented for bulk materials. In more recent work, Löwdin Downfolding has been combined with Quantum Monte Carlo to help significantly reduce the sign problem in quantum chemistry calculations.[65] It has also played a role in deriving tight-binding models for superconducting systems[13] and monolayers of transition-metal dichalcogenides[57].

The basis of Löwdin Downfolding is the partitioning of the Hamiltonian into two blocks: the “target” block which defines the space of the effective model and its complementary block containing all the remaining degrees of freedom. The goal is then to transform the complementary block to the target space and absorb it into the target block. Given a Hamiltonian  $\mathcal{H}$  with eigenstate  $\Psi$  and a complete orthonormal basis  $\{\Phi_n\}$ , we can partition the basis into a target space denoted by  $P$  and its complementary space,  $Q$ . Then expanding  $\mathcal{H}$  and  $\Psi = \sum_n C_n \Phi_n$  in these two spaces, we can express the full Hamiltonian and eigenstate as

$$H = \begin{pmatrix} H_{PP} & H_{PQ} \\ H_{QP} & H_{QQ} \end{pmatrix}, \quad C = \begin{pmatrix} C_P \\ C_Q \end{pmatrix} \quad (1.7)$$

For an eigenstate of energy  $E$ , the Schrödinger equation reads

$$\begin{pmatrix} H_{PP} & H_{PQ} \\ H_{QP} & H_{QQ} \end{pmatrix} \begin{pmatrix} C_P \\ C_Q \end{pmatrix} = E \begin{pmatrix} C_P \\ C_Q \end{pmatrix} \quad \Rightarrow \quad \begin{aligned} H_{PP}C_P + H_{PQ}C_Q &= EC_P \\ H_{QP}C_P + H_{QQ}C_Q &= EC_Q \end{aligned} \quad (1.8)$$

Then solving for  $C_Q$  in the second equation and substituting it into the first, we arrive at

$$\begin{aligned} (H_{PP} + H_{PQ}(E\mathbb{1}_Q - H_{QQ})^{-1}H_{QP})C_P &= EC_P \\ \Rightarrow H_{eff} &= H_{PP} + H_{PQ}(E\mathbb{1}_Q - H_{QQ})^{-1}H_{QP} \end{aligned} \quad (1.9)$$

where  $\mathbb{1}_Q$  is the identity matrix spanning the complimentary space,  $Q$ .

Looking at the form of (1.9), we can see the first term is just the projection of the original Hamiltonian into the target space followed by a correction in the second term coming from the complementary space. This is equivalent to how the low-energy Hamiltonian in section 1.1 is dressed with the effects coming from expanding in the screened interaction. Similarly, just as the dressing promotes the one and two-body interactions to being frequency dependant in the three-stage approach, so too does the effective Hamiltonian in the Löwdin scheme come with an energy dependence.

It should be noted that the contributions from the complimentary space involve a seemingly complicated calculation involving the inversion of a potentially large matrix. The complexity is controlled by the choice of basis  $\{\Phi_n\}$  and depending on the approach used, can vary in size. When directly applied to molecular systems, a large but limited basis set can be used to parameterize the Hamiltonian. Then applying perturbation theory up to some order, the second term in (1.9) can be approximately calculated.[19] Other applications are concerned with deriving tight-binding models within the space of a reduced set of orbitals in order to get an effective model. In these cases, the Hamiltonian is parameterized by a set of orbitals resulting from a DFT calculation. Within this single-particle framework, the Hamiltonians can be small enough to be handled directly, making the effective model in (1.9) easy to calculate.[13, 57]

In principle, this approach should yield useful effective models when defined over the many-particle Hilbert space as no approximations are needed before applying the Löwdin scheme.

This of course comes with the obvious difficulty of working directly in this exponentially large space and calculating inverses are large (and possibly infinite) matrices. On the other end of the spectrum, using this technique in a single-particle framework as discussed above makes it more malleable, but now we are at the mercy of the approximations that are inherent to DFT methods and other single-particle approaches.

## 1.2.2 Canonical Transformations

Another approach used to arrive at an effective Hamiltonian is based on Jacobi Canonical Transformations (CT), which are traditionally used in computer diagonalization routines for Hermitian matrices. Given a Hermitian matrix  $H$  with a non-zero off-diagonal element  $H_{ij}$ , the Jacobi CT constitutes a unitary transformation

$$U = e^{-A}, \quad A = -A^\dagger \tag{1.10}$$

such that  $U^\dagger H U$  yields a new matrix  $\tilde{H}$  with the  $ij^{\text{th}}$  element removed and rotated into the remaining matrix elements. Repeated applications of  $U$  targeting the other off-diagonal pieces will then result in a fully diagonal matrix.

This procedure can be generalized to act directly on the second-quantized Hamiltonian to derive simpler effective models with diagonal interactions[70] or more, specifically, on Hamiltonians derived for quantum chemistry to include renormalization effects coming from higher-order bands[71]. Focusing on the latter case, we follow the familiar first step of partitioning the original Hamiltonian into low and high energy spaces

$$\hat{\mathcal{H}} = \hat{\mathcal{H}}_L + \hat{\mathcal{H}}_{LH} + \hat{\mathcal{H}}_H \tag{1.11}$$

These are also sometimes referred to as the “active” and “external” spaces, respectively.

The goal of CT is to then rotate the dynamical correlations with the external space into the Hamiltonian defined over only the active space

$$\tilde{\mathcal{H}} = e^{\hat{A}} \hat{\mathcal{H}} e^{-\hat{A}}, \quad \tilde{\mathcal{H}} = \hat{\mathcal{H}} + [\hat{\mathcal{H}}, \hat{A}] + \frac{1}{2} [[\hat{\mathcal{H}}, \hat{A}], \hat{A}] + \dots \quad (1.12)$$

where the transformation is calculated term by term using the Baker-Campbell-Hausdorff(BHC) expansion. Individual off-diagonal elements in  $\mathcal{H}$  can be targeted by choosing particular excitation operators,  $\hat{\gamma}_\alpha$ , to construct the anti-Hermitian operator  $\hat{A}$ . For example, we can choose  $\hat{\gamma}_1 = \hat{c}_{a_1}^\dagger \hat{c}_{a_2}^\dagger \hat{c}_{e_1} \hat{c}_{e_2}$  where the indices  $a_1, a_2$  denote two arbitrary states in the active space and  $e_1, e_2$ , two arbitrary states in the external space. Multiple excitations can be targeted which is equivalent to writing  $\hat{A}$  as a linear combination over the corresponding excitation operators

$$\hat{A} = \sum_{\alpha} A_{\alpha} \hat{\gamma}_{\alpha} . \quad (1.13)$$

Note that  $\hat{\gamma}_{\alpha}$  are in general many-body excitations(one-, two-, three-body, etc. operators). We can then find the coefficients  $\{A_{\alpha}\}$  such that

$$\langle \Psi_L | \tilde{\mathcal{H}} \hat{\gamma}_{\alpha} | \Psi_L \rangle = 0 \quad (1.14)$$

for each off-diagonal term,  $\alpha$ . Using the Hermiticity of  $\tilde{\mathcal{H}}$ , we can rewrite these equations as

$$\langle \Psi_L | \left[ \tilde{\mathcal{H}}, \hat{\gamma}_{\alpha} - \hat{\gamma}_{\alpha}^\dagger \right] | \Psi_L \rangle = 0 \quad (1.15)$$

which have been studied and are known as the generalized Brillouin conditions.[34] After using (1.15) to find the transformation  $e^{\hat{A}}$ , we can then use the BHC expansion to calculate the new effective Hamiltonian up to the desired order.

One limitation of CTs that is relevant to this work is its inability to further reduce the range of the diagonal two-body terms. In a best-case scenario, the two-body interactions of a Hamiltonian may be reduced to pure density-density interactions corresponding to the diagonal elements in the many-body matrix. If one seeks to derive an effective model with an on-site interaction instead, this technique cannot be applied since it only works to remove off-diagonal elements.

### 1.3 Fitting Reduced Hamiltonians to Accurate Simulations

The *ab initio* methods discussed so far have departed from the simplicity involved in fitting model Hamiltonians to experimental data in empirical and semi-empirical downfolding techniques. Of course in these cases, the main disadvantage is the lack of experimental data for the particular system in question, including relevant observables needed in order to derive specific model parameters. If one instead uses the results of an approximate, but sufficiently accurate many-body calculation to find the relevant observables, then one can leverage the simplicity of fitting model Hamiltonians to real systems without the need for experimental data.

In general, the effective model may be written as a sum over  $n$ -body operators with corresponding rank- $2n$  tensors representing the couplings. The values of the coefficients are then optimized by matching various quantities between the real system and model Hamiltonian. For any typical system, the higher-order  $n$ -body terms are too expensive to calculate to arbitrary order, so in practice, the effective model is made up of one and two-body terms. Truncating the higher-order contributions to the Hamiltonian is an approximation, but when applied to bulk systems, the one and two-body operators can be sufficient enough to capture



the low-energy physics to some satisfactory degree of accuracy. This is the main approach taken by [12] and later formalized in [73] which is dubbed “Density Matrix Downfolding”. Although this is by no means the only fitting technique, it provides an improved framework based on density matrices that is relevant to the work in this thesis.

### 1.3.1 Density Matrix Downfolding

Just as in the previous sections, the goal here is to first identify a target space and downfold the Hamiltonian  $\mathcal{H}$  defined in the original space to  $H_{eff}$  defined in the target space. The mapping between these two spaces is defined by a set of Wannier functions  $\{w_i\}$ , which may be constructed from a reduced set of DFT orbitals as in the three-stage downfolding approach discussed in section 1.1. Keeping all terms up to two-body operators, the effective model takes the form

$$H_{eff} = C + \sum_{ij} t_{ij} c_i^\dagger c_j + \sum_{ijkl} V_{ijkl} c_i^\dagger c_j^\dagger c_k c_l \quad (1.16)$$

where  $C$  is some constant energy shift. In any general fitting technique, the parameters  $\{t_{ij}\}$  and  $\{V_{ijkl}\}$  are found by variationally minimizing a cost function which attempts to match expectation values of certain quantities between  $\mathcal{H}$  and  $H_{eff}$  with respect to a set of  $N$  states defined in a low-energy space. Density Matrix Downfolding(DMD) identifies these important quantities as the energy spectra and reduced density matrices(RDMs).

In order to define the cost function, the results of an *ab initio* many-body calculation are used to obtain the energy and RDM for a set of the  $N$  lowest eigenstates of  $\mathcal{H}$ . An analogous set of quantities for  $H_{eff}$  is obtained by a similar calculation with initial guesses for the Hamiltonian parameters  $\{t_{ij}\}$  and  $\{V_{ijkl}\}$ . We then define the cost function by summing the

mean-square error between the quantities in  $\mathcal{H}$  and  $H_{eff}$  state by state

$$\mathcal{E} = \sum_s (E_s^a - E_s^m)^2 + \lambda \sum_s \sum_{ijkl} \left( \langle c_i^\dagger c_j^\dagger c_k c_l \rangle_s^a - \langle c_i^\dagger c_j^\dagger c_k c_l \rangle_s^m \right)^2 \quad (1.17)$$

where the value  $\lambda$  controls the degree to which the two-particle RDMs are matched. The subscript  $s$  indicates expectation values measured with respect to state  $s \in N$  and the superscripts  $a$  and  $m$  denote quantities from  $\mathcal{H}$  and  $H_{eff}$ , respectively. Note that in the second term, the summation over  $ijkl$  enumerates the sites of  $H_{eff}$  defined in the target space meaning that the two-particle RDM of  $\mathcal{H}$  must first be transformed into this basis using the Wannier functions  $\{w_i\}$  in order to properly compare the values. Once the cost function is defined, any gradient-free numerical optimization algorithm may be used to find the set of  $\{t_{ij}\}$  and  $\{V_{ijkl}\}$  that minimizes  $\mathcal{E}$ . Since the eigenstates need to be determined for the model before the expectation values are calculated,  $H_{eff}$  needs to be re-diagonalized every time any of the model parameters change, that is, for each function call during the optimization.

There are several drawbacks inherent to this approach that can hinder its application to arbitrary systems. First, the choice of the *ab initio* many-body method can affect the accuracy of the eigenstates used to calculate the target energies and RDMs. If we use a highly accurate technique, we may be limited to calculations on small system sizes whose downfolded parameters may not correspond to those at larger system sizes. And if instead a low accuracy technique is used to simulate the full system at larger system sizes, the resulting energies and RDMs to which the effective model is fitted may not be representative of the true low-lying energy space. Second, if the *ab initio* method limits the number of eigenstates that can be accurately recovered from the low-energy space, we may not have enough states to fully describe the space.

Suppose instead that rather than restricting ourselves to using eigenstates, we used any

state so long as it's within the low-energy space we are targeting. The idea is that if the two Hamiltonians  $\mathcal{H}$  and  $H_{eff}$  behave in the same way for any set of arbitrary states, then they should also do so for eigenstates. By removing the restriction of targeting a particular set of states, we alleviate the need for accurately producing the target energies and RDMs and just take whatever states we get so long as they are within the energy window of interest. This shifts the focus from using highly accurate methods to using methods which can easily sample low-energy states. In practice, this turns out to work very well and forms the basis of modern DMD.

In addition to using an arbitrary set of low-lying states, we can eliminate the need to re-diagonalize  $H_{eff}$  for each function call by imposing that the one and two-particle RDMs for the effective model correspond exactly to those from the *ab initio* calculation, but transformed into the target space using the Wannier functions. Applying this assumption to the energies  $E_s^m$

$$\begin{aligned}
E_s^m &= \langle H_{eff} \rangle_s = C + \sum_{ij} t_{ij} \langle c_i^\dagger c_j \rangle_s^m + \sum_{ijkl} V_{ijkl} \langle c_i^\dagger c_j^\dagger c_k c_l \rangle_s^m \\
&\approx C + \sum_{ij} t_{ij} \langle c_i^\dagger c_j \rangle_s^a + \sum_{ijkl} V_{ijkl} \langle c_i^\dagger c_j^\dagger c_k c_l \rangle_s^a
\end{aligned} \tag{1.18}$$

and substituting into (1.17), the second term vanishes and we can rewrite the mean-squared

error of the energies as a system of linear equations

$$\begin{pmatrix} E_1^a \\ E_2^a \\ E_3^a \\ \vdots \\ E_N^a \end{pmatrix} = \begin{pmatrix} 1 & \dots & \langle c_i^\dagger c_j \rangle_1^a & \dots & \langle c_i^\dagger c_j^\dagger c_k c_l \rangle_1^a & \dots \\ 1 & \dots & \langle c_i^\dagger c_j \rangle_2^a & \dots & \langle c_i^\dagger c_j^\dagger c_k c_l \rangle_2^a & \dots \\ 1 & \dots & \langle c_i^\dagger c_j \rangle_3^a & \dots & \langle c_i^\dagger c_j^\dagger c_k c_l \rangle_3^a & \dots \\ \vdots & \vdots & \vdots & \vdots & \vdots & \vdots \\ 1 & \dots & \langle c_i^\dagger c_j \rangle_N^a & \dots & \langle c_i^\dagger c_j^\dagger c_k c_l \rangle_N^a & \dots \end{pmatrix} \begin{pmatrix} C \\ \vdots \\ t_{ij} \\ \vdots \\ V_{ijkl} \\ \vdots \end{pmatrix}$$

$$\Rightarrow \mathbf{E} = A\mathbf{x} \tag{1.19}$$

By using the singular value decomposition of the matrix  $A$ , we can invert it and solve for the Hamiltonian parameters defined in  $\mathbf{x}$  in a single step.

The procedure described above has been applied to complex systems such as the Hydrogen chain, Graphene and Hydrogen honeycomb lattice as well as molecular systems such as diatomic FeSe. In all of these cases, the resulting effective models are compared to many-body calculations from Variational Monte Carlo (VMC) and Diffusion Monte Carlo (DMC). [73]

## Chapter 2

# DMRG Methods for Electronic Structure

Historically, the main approach to many quantum chemistry problems has been DFT or combinations of other many-body methods with DFT such as Dynamical Mean-Field Theory and GW. These approaches perform very well for small systems with weak to moderate electron correlations, but begin to break down in the presence of strong correlations. In this regime, Quantum Monte Carlo methods such as Variational Monte Carlo and Diffusion Monte Carlo can be implemented for very large system sizes at high accuracy, but are limited in their applicability due to the infamous sign problem. Algorithms such as the Density Matrix Renormalization Group(DMRG) can operate in this regime without the sign problem, allowing accurate calculations of strongly-correlated systems at large system sizes, but quickly becomes intractable for systems with much higher entanglement. Surveying the available quantum many-body methods, we find a gap in the applicability of these techniques to large systems with high entanglement. Reaching this regime is a matter of improving any of the previously mentioned approaches and in what follows, we discuss the work that has already been done in taking the first steps at bringing DMRG into this realm of applicability.

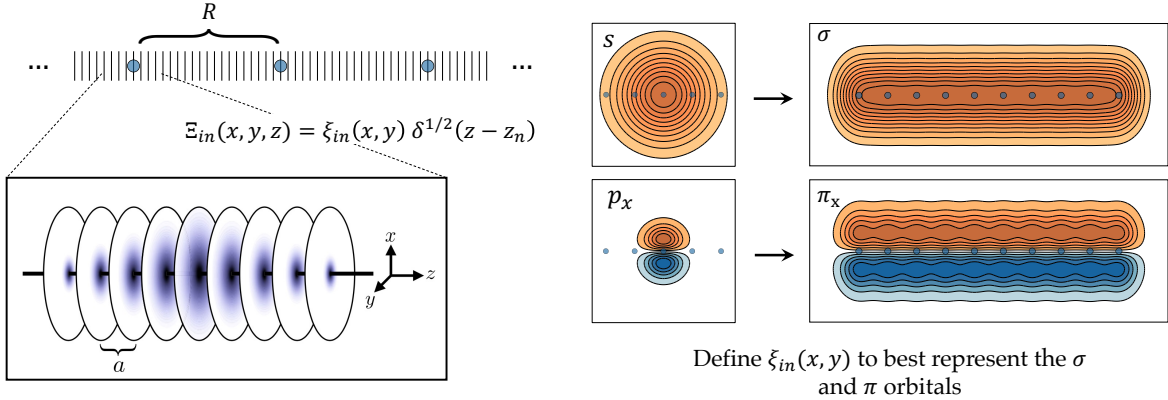


Figure 2.1: A schematic representation of the sliced-basis functions for systems arranged in a 1D chain geometry. The atoms are represented by the small blue circles with atomic spacing  $R$ . On the left, the grid points along the chain are shown which when zoomed in shows a cartoon of the slices separated by a distance  $a$ . On the right, the usual spherically-symmetric Gaussian basis functions are generalized to cylindrical symmetry which the sliced-basis is designed to capture.

## 2.1 Sliced-Basis DMRG

Adapting DMRG to real systems requires parameterizing the continuous degrees of freedom into localized “sites” with a locally defined Hilbert space. In the conventional approach the sites are formed by transforming the original Hamiltonian into a particular basis, typically a linear combinations of Gaussian basis functions. A severe drawback of this approach is the large number of two-electron terms in the resulting Hamiltonian, scaling as  $N_b^4$ , where  $N_b$  is the number of basis functions. This stems from the large overlap of the basis functions, which are, in most cases, required to extend over the entirety of the system in order to correctly capture all the correlations. If one instead used a real-space grid representation, with  $N_g$  being the number of grid points, one gets  $N_g^2$  interaction terms but at the cost of having  $N_g \gg N_b$ . Sliced bases are a compromise, with favorable scaling for the interactions and an intermediate number of sites[64].

In sb-DMRG we use a real-space grid along one direction and a localized set of 2D Gaussian basis functions spanning the other two transverse directions, defining a “slice” at each grid

point(see Fig. 2.1 for a schematic representation). This is particularly advantageous when dealing with systems extending much more in one direction than in the transverse direction, such as chains of atoms. The entanglement of the system in the sliced basis is favorable, not much above that of the corresponding effective Hubbard model. In contrast, sets of conventional basis functions must be localized before being used in DMRG, since extended molecular orbitals can give rise to volume-law entanglement scaling, which becomes dominant on long chains.

In addition to maintaining an area-law entanglement scaling, restricting these functions to slices makes each function orthogonal to all other functions not on the same slice, reducing the number of interaction terms from quartic to quadratic in the number of grid points. The resulting long-range Coulomb interactions may then be compressed via an SVD scheme to produce an matrix product operator with a modest bond dimension which is nearly independent of system size[11, 52]. This technique allows the method to scale essentially linearly with the number of atoms, making large chains of atoms accessible to DMRG-level accuracy.

### 2.1.1 Constructing the Sliced-Basis Functions

Fig. 2.1 gives a schematic overview of how the sliced-basis functions are constructed. The 2D transverse functions defining the slices are taken from standard 3D Gaussian basis set functions defined by four numbers,  $(\zeta, n, m, k)$  with each function taking the form

$$g(x, y, z) = x^n y^m z^k e^{-\zeta(x^2+y^2+z^2)} \tag{2.1}$$

The values of  $n$ ,  $m$  and  $k$  determine the character of the function(i.e.  $s$ -type,  $p$ -type etc.) and  $\zeta$  controls the width. Some of these primitive Gaussians (especially the  $s$  functions) are contracted with others of the same type to form new contracted basis functions. Therefore

in the most general case, the 3D parent basis set is defined by

$$\Phi_i(x, y, z) = \sum_j c_{ij} g_j(x - x_A, y - y_A, z - z_A) \quad (2.2)$$

where  $\{c_{ij}\}$  are the contraction coefficients and  $\mathbf{r}_A = (x_A, y_A, z_A)$  denotes the position of atom  $A$ . For a system whose atoms are arranged along a 1D chain, the spherical symmetry of the original Gaussians translates to a cylindrical one, taking  $s$  orbitals to  $\sigma$  orbitals and  $p$  orbitals to  $\pi$  orbitals, etc. Therefore we would like to define our basis as one that best captures functions of the form

$$\Phi_i(x, y, z) = \sum_{jA} c_{ij} g_j(x, y, z - z_A) \quad (2.3)$$

which is now restricted to a chain along the  $z$ -axis with an extra summation over the atoms.

Choosing the grid to go along the  $z$ -axis, we then define the sliced basis as a set of orthonormal functions

$$\Xi_{in}(x, y, z) \equiv \xi_{in}(x, y) \delta^{1/2}(z - z_n) \quad (2.4)$$

such that on each slice at  $z_n$ , the transverse functions  $\{\xi_{in}\}$  form an orthonormal set. For now, we do not worry about the particular form of  $\{\xi_{in}\}$ . Later we will see that there is a natural choice for these transverse functions that accurately captures orbitals of the form (2.3). Without loss of generality, we may choose  $n = m = k = 0$  ( $s$ -type) for the Gaussians in (2.3) to keep the notation simple. Expanding these functions in terms of the basis (2.4),



the  $i^{\text{th}}$  parent functions for slice  $n$  at position  $z_n$  can be written as

$$\begin{aligned}\phi_i^n(x, y) &= \sum_{jkA} c_{ij} e^{-\zeta_j(z_n - z_A)^2} d_{jk} \xi_k(x, y), \quad d_{jk} = \int dx dy g_j(x, y) \xi_k(x, y) \\ &= \sum_k \eta_{ik}^n \xi_k(x, y), \quad \eta_{ik}^n \equiv \sum_{jA} c_{ij} e^{-\zeta_j(z_n - z_A)^2} d_{jk}\end{aligned}\tag{2.5}$$

We then use Löwdin orthogonalization to derive an orthonormal basis set from  $\{\phi_i\}$ . Since  $\{\xi_k\}$  already form an orthonormal set, the overlap matrix is given by the outer product of the coefficient matrix  $\eta_n$

$$\rho_{ii'}^n = \sum_k \eta_{ik}^n \eta_{i'k}^n\tag{2.6}$$

which upon diagonalization yields

$$\rho_{ii'}^n = \sum_k U_{ik}^n D_{kk}^n U_{ki'}^{\dagger n}\tag{2.7}$$

$$\Rightarrow \rho_n^{-1/2} = U_n D_n^{-1/2} U_n^\dagger\tag{2.8}$$

Using  $\rho_n^{-1/2}$  to transform  $\{\phi_i^n\}$  and noting that we can write  $\eta = U_n D_n^{1/2}$ , the sliced-basis functions can be expressed as

$$\phi_i^n(x, y) = \sum_k U_{ik}^n \xi_k(x, y)\tag{2.9}$$

Due to the unitarity of  $U$  and orthonormality of  $\xi$ , the above set of functions are orthonormal on each slice as desired. What's more is that the elements of  $D$  in (2.7) can be used as a criteria for truncated the basis in a controlled way.

Thus far, we have kept the definition of  $\{\xi_i\}$  arbitrary and have only used the fact that they form an orthonormal set. But as previously mentioned, there is a particular choice which is natural for the type of problems sb-DMRG is targeting. More specifically, this basis is

ideally suited for system with a chain-like geometry. And so the spherical symmetry of the original 3D Gaussians should be transformed to a cylindrical one, taking  $s$ -type functions to  $\sigma$ -type,  $p$ -type functions to  $\pi$ -type, etc. This can be done by defining  $\{\xi_i\}$  to be a set of orthogonalized 2D Gaussians—the same ones used in the original definition of  $\Phi$ , but projected to the  $x$ - $y$  plane of the local slice.

Again, following the prescription of Löwdin orthogonalization, we calculate the overlap matrix between the 2D Gaussians on a slice

$$G_{ij} = \int dx dy g_i(x, y) g_j(x, y) \quad (2.10)$$

and define the functions  $\{\xi_i\}$  as

$$\xi_i(x, y) = \sum_j G_{ij}^{-1/2} g_j(x, y) \quad (2.11)$$

Substituting these into (2.9), we arrive at an orthonormal sliced-basis defined in terms of 2D Gaussian basis functions

$$\begin{aligned} \phi_i^n(x, y) &= \sum_{kl} \left( U_{ik}^n G_{kl}^{-1/2} \right) g_l(x, y) \\ &= \sum_l f_{il}^n g_l(x, y), \quad f_{il}^n = \sum_k U_{ik}^n G_{kl}^{-1/2} \end{aligned} \quad (2.12)$$

To see the how one can recover the  $\sigma$  functions from this formulation, let us consider the case of using uncontracted,  $s$ -type Gaussians as our original 3D parent basis. Leaving the functions uncontracted is equivalent to setting  $c_{ij} = \delta_{ij}$  in (2.5) and with the definition of  $\xi_i$  in (2.11), the coefficients  $\{\eta_{ik}^n\}$  in (2.5) are reduced to

$$\eta_{ik}^n = \sum_A e^{-\zeta_i(z_n - z_A)^2} G_{ik}^{1/2} \quad (2.13)$$

and we can express the basis functions as

$$\phi_i^n(x, y) = \sum_{kA} \left( e^{-\zeta_i(z_n - z_A)^2} G_{ik}^{1/2} \right) \xi_k(x, y) \quad (2.14)$$

This can easily be made into an orthonormal set by transforming  $\{\phi_i^n\}$  with  $G_{ii}^{-1/2} \left( \sum_A e^{\zeta_i(z_a - z_A)^2} \right)^{-1}$  and summing over  $k$  which is no more than using the orthogonalized 2D Gaussians to form the sliced-basis functions. The widths of these functions are independent of their proximity to the atoms, giving  $\sigma$ -function character to the functions representing the chain. This also generalizes to  $p$ -type Gaussians which give  $\pi$ -functions, etc.

In the most general sliced-basis, the Hamiltonian takes the form

$$H = \frac{1}{2} \sum_{nn'} \sum_{ij} t_{ij}^{nn'} c_{ni\sigma}^\dagger c_{n'j\sigma'} + \frac{1}{2} \sum_{nn'} \sum_{ijkl} V_{ijkl}^{nn'} c_{ni\sigma}^\dagger c_{n'j\sigma'}^\dagger c_{n'k\sigma'} c_{nl\sigma} \quad (2.15)$$

where  $n, n'$  enumerate the slices,  $i, j, k, l$ , the local orbitals and  $\sigma, \sigma'$  the spins (spin summation implied in the above notation). Here, the total number of interaction terms is  $N_z^2 N_g^4$  where  $N_z$  is the number of slices (i.e. grid points in the  $z$ -direction) and  $N_g$ , the number of local basis functions on each slice. Note that  $N_g \ll N_z$  which means the scaling is dominated by the system length. In the limit that  $N_g = 1$ , the resulting Hamiltonian takes a very simple form with only  $N_z^2$  density-density interactions.

## 2.1.2 Compressing the Long-Range Interactions

The interaction terms in (2.15) come from the  $1/r$  Coulomb interaction and therefore stretch over the entire system. When representing these terms with a Matrix Product Operator (MPO), the bond dimension begins to scale with the system size, becoming very costly for large systems. To improve the efficiency of sb-DMRG, the interactions are compressed through a Singular Value Decomposition (SVD) scheme which greatly reduces the bond di-

mension of the resulting MPO. Here we sketch an intuitive example that demonstrates the compression, but refer the reader to the supplementary material of Stoudenmire and White[64] for the details.

Although the compression algorithm can be applied directly to the interaction terms in (2.15), let's consider the simplest case in which we only have one basis function per slice for clarity. The interaction terms can then be simplified to

$$\sum_{n \leq n'} V_{nn'} \hat{n}_n \hat{n}_{n'} \quad (2.16)$$

These interaction will decay as  $1/|n - n'|$ , but in practice it is best to represent the power-law decay as a sum of Gaussians by a fitting procedure. This not only simplifies the interaction integrals by making them integrals of products of Gaussians (for a Gaussian sliced-basis set), but also allows the interactions to factorize, taking full advantage of the SVD compression.

Take, for example, the case in which the interactions decay exponentially and are given by

$$V_{nn'} = \lambda^{|n-n'|} . \quad (2.17)$$

Restricting ourselves to the  $k^{\text{th}}$  upper-right block of  $V$ —that is the matrix formed by taking the elements from some diagonal  $V_{kk}$  to the upper-right corner at  $V_{1N}$ —constrains  $n' \geq n$ , allowing us to factorize the interaction as

$$V_{nn'} = \lambda^{|n-n'|} = \lambda^{n'-n} = \lambda^{n'} \lambda^{-n} \quad (n' \geq n) . \quad (2.18)$$

The last term in the above expression represents an outer product between two vectors which forms a rank-1 matrix when multiplied. This is the most optimal compression that can be achieved through an SVD. If we then continue in this fashion and represent each of the upper-right blocks of  $V$  by a set of truncated matrices, we can write the MPO in terms of

this compressed representation yielding a bond dimension that's independent of the system size.

## 2.2 sb-DMRG on Hydrogen Chains

Once the system is expressed in the form (2.15), standard DMRG can be used to obtain the wavefunction. Given the size and complexity of this Hamiltonian relative to traditional lattice models, a few key features may be added in order to improve the efficiency of the calculation. Here we discuss the main ingredients that are implemented in order to achieve this boost in performance.

### 2.2.1 Initializing sb-DMRG with Hartree-Fock

A typical DMRG calculation begins by initializing the wavefunction into a Néel state containing the desired number of spin-up and spin-down particles. Each iteration of DMRG (called a sweep) then grows the entanglement in a controlled way until the wavefunction approximates the exact ground state to the desired accuracy. For lattice models such as the Hubbard or Heisenberg models at half-filling, the ground state can quickly be recovered with only a few sweeps (5-15, depending on system size). But when computing the ground state of the hydrogen chain (H-chain), more sweeps are usually required, with each sweep taking more compute time.

A simple solution is to replace the Néel state ansatz with one from a Hartree-Fock (HF) calculation, leaving DMRG to build up only the pieces of the wavefunction that contribute to the correlation energy rather than constructing the entire many-body structure from scratch. Since HF calculations are much faster than DMRG, using a low-accuracy initial guess can significantly speed-up the overall performance without sacrificing accuracy.

After casting the original H-chain Hamiltonian into the sliced basis, we first run HF to recover the single-particle states,  $\{\theta_\alpha\}$ , that make up the HF wavefunction. For a chain with  $N_a$  atoms at half-filling, the ground state can be expressed in Fock space as

$$|\Psi_0\rangle = d_{N_a,\downarrow}^\dagger d_{N_a-1,\downarrow}^\dagger \dots d_{1,\downarrow}^\dagger d_{N_a,\uparrow}^\dagger d_{N_a-1,\uparrow}^\dagger \dots d_{1,\uparrow}^\dagger |0\rangle \quad (2.19)$$

where the Fock operators  $\{d_{\alpha,\sigma}^\dagger\}$  are defined variationally from HF in terms of the sliced-basis operators  $\{c_{ni,\sigma}^\dagger\}$  as

$$d_{\alpha,\sigma}^\dagger = \sum_{ni} \theta_\alpha^{ni} c_{ni,\sigma}^\dagger. \quad (2.20)$$

Here  $\alpha$  enumerates the Fock state,  $n$  the slice,  $i$  the local orbital on slice  $n$  and  $\sigma$ , the spin (note here that since the system is at half-filling, the HF coefficients,  $\{\theta_\alpha\}$ , are the same for spin-up and spin-down). Each of these Fock operators may be written as a matrix product operator (MPO), a tensor network representation of a quantum many-body operator which can then act successively on the vacuum state. The end result is a many-body HF wavefunction written as a matrix product state (the tensor network representation of a many-body wavefunction) which can be directly used as a starting state in DMRG.

## 2.2.2 Reducing to Slice Natural Orbitals

As we saw in the previous section, the number of interaction terms for the sliced-basis Hamiltonian scales as  $N_z^2 N_g^4$  where  $N_z$  is the number of slices and  $N_g$ , the number of local basis functions per slice. Although  $N_g \ll N_z$ , the number of interaction terms may be drastically reduced by decreasing  $N_g$ . For example, the standard CC-pVDZ basis set containing six Gaussians contracted down to four can have  $4^4 = 256$  times less interactions terms if reduced to a single effective basis function per slice. Therefore it is highly desirable to make  $N_g$  as small as possible while still maintaining an acceptable degree of accuracy.

Lets consider the case of using the CC-pVDZ basis set to describe the H-chain. The basis set has two  $s$ -type and two  $p$ -type functions for a total of four functions per slice. Now, suppose we are in an insulating phase of the H-chain where we expect the electronic structure to be mainly of  $s$  character. In this regime, the  $p$  functions in the basis set should play a minor role and we expect that they may be removed. To check, we can run sb-DMRG in the full basis set and form a single-body reduced density matrix on a slice defined as

$$C_{ij} = \langle c_i^\dagger c_j \rangle, \quad \text{for } \{i, j\} \in [1, N_g] \quad (2.21)$$

where  $i, j$  are restricted to live on the same slice. The matrix  $C$  will be block diagonal with a total of three blocks, one for  $s$ , one for  $p_x$  and one for  $p_y$ . After diagonalizing  $C$ , we can inspect the eigenvalues to determine which of the four single-particle states, also referred to as “slice natural orbitals” (SNOs), are the most active and truncate those that have small eigenvalues. If the truncated states have occupancies which are sufficiently small, the resulting slice density matrix will be approximately preserved. We can then define a basis transformation from the full  $N_g$  CC-pVDZ basis functions to the  $N_o < N_g$  SNOs, giving a Hamiltonian with  $N_o$  functions per slice. The resulting Hamiltonian is then be fed back into another sb-DMRG routine to obtain the final ground state.

Note that in reducing the number of basis functions, we required the slice density matrix from an sb-DMRG calculation in the full basis. This may seem counter-productive, but in fact the original calculation need not be fully converged and can instead be used well before the wavefunction closely approximates the true ground state. In addition, the basis may be expanded during any point in the calculation through a simple basis transformation so that more information can be incorporated into the resulting SNOs. As we will see in the next few chapters, the H-chain Hamiltonians are frequently reduced to one and two basis functions per slice with little loss of accuracy.

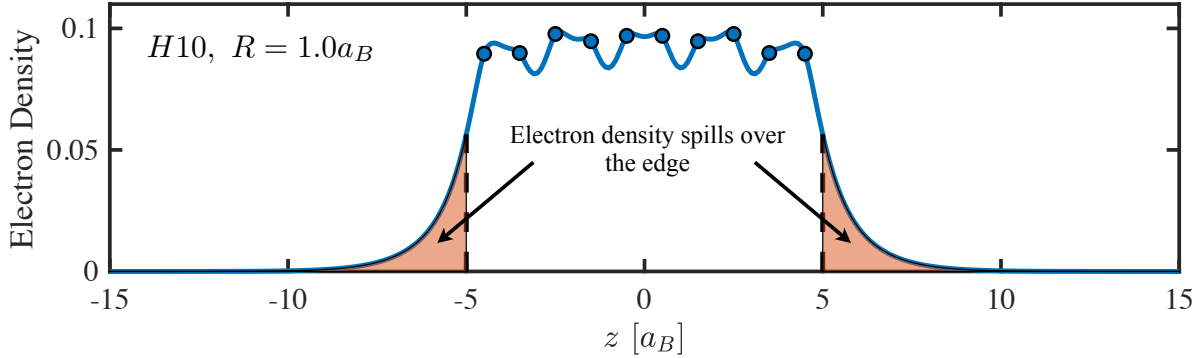


Figure 2.2: Ground state electron density for H10 at  $R = 1.0a_B$ . The regions filled in with red represent the end spill-off of the electron density due to the large empty regions on either side of the chain.

### 2.2.3 Boundary Conditions

As a final added feature, we consider the boundary conditions to be used in an H-chain calculation. In a real hydrogen chain, the tail of the electronic wavefunction extends a moderate distance beyond the nuclei that make up the chain. However when treating the finite chain as a segment of an infinite chain, the electrons should no longer be allowed to spread beyond the finite segment, since the other atoms that make up the larger, infinite chain obstruct them from doing so. Without taking this effect into account, the end spill-off of the electrons shown in Fig. 2.2 will result in a reduction of the bulk electron density, slowing the convergence to the thermodynamic limit. Although this effect is very minor at large atomic spacing,  $R$ , it becomes important for sufficiently small  $R$ , and results in a reduction in  $R_c$  for shorter chains[48]. If periodic boundary conditions are used, this boundary effect does not occur, but periodic boundaries slow the convergence of DMRG. Instead, we can use hard walls placed at a distance  $R/2$  beyond the first and last atoms in order to mimic the presence of other atoms that would otherwise be there in the infinite chain. While there are still some edge effects, we will find that they are much smaller than with open ends.



# Chapter 3

## The Hydrogen Chain

As used in this work, the hydrogen chain (H-chain) consists of  $N$  protons and electrons. The protons are held fixed and are equally spaced by a distance  $R$ , defining a static, periodic potential for the system. Chemically, H-chains would be unstable, but for electronic structure calculations they are realistic in the sense of having three dimensional electron wavefunctions with long range Coulomb interactions. Most importantly, it can be regarded as a realistic model of a 1D solid, with an interesting phase diagram as one varies  $R$  as shown in Fig. 3.1(b). Despite its apparent complexity, the H-chain remains accessible to a whole host of modern many-body methods[47, 48, 22, 66, 39, 59], including DMRG methods. Along with its rich physics, the H-chain can be tuned to resemble simple lattice models, such as the Hubbard and Heisenberg model, providing a smooth connection between a realistic 1D solid and fundamental theoretical models. These features, together with its computational tractability, make the H-chain an excellent candidate to study the progression from a real system to an effective model.

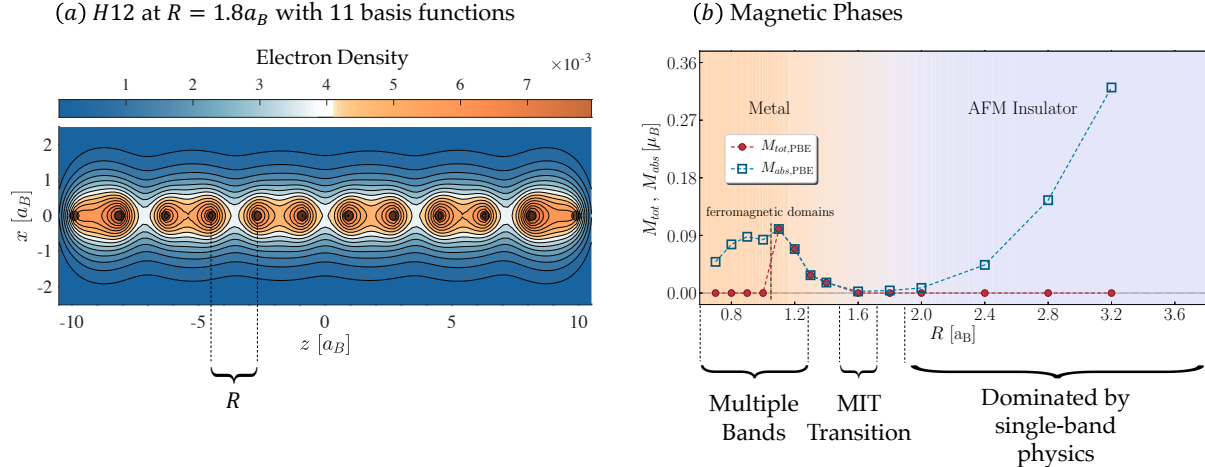


Figure 3.1: Ground state electron structure and magnetic phases of the H-chain. (a) sb-DMRG calculation with 11 basis functions for H12 at  $R = 1.8a_B$ . There is a very apparent dimerization of the electrons. (b). Magnetic phases from DFT-PBE taken from [48]. Here  $M_{\text{tot}} = \int d^3r m(r)/N$  and  $M_{\text{abs}} = \int d^3r |m(r)|/N$  where  $m(r)$  is the magnetization of the simulation cell.

### 3.1 Ground State Properties

The correlations within the H-chain are controlled by a single parameter,  $R$ , the atomic spacing. In a localized atomic orbital picture,  $R$  controls the degree of overlap between neighboring orbitals which in turn determines the hopping strength. At small  $R$ , the orbitals heavily overlap leading to more hopping which, in the extreme limit, begins to resemble a 1D electron gas. As  $R$  is increased, the lack of overlap between neighboring atoms suppresses the hopping, leading to a more insulating state. This is the standard scenario for a Mott metal-insulator transition, although the 1D nature of the chain can alter the expected physics.

For  $R > 1.8a_B$ , the physics is mainly dominated by a single band composed primarily of the atomic  $1s$  orbitals, with higher orbitals playing an increasingly more minor role as the atomic spacing is increased. In this regime, the electrons exhibit quasi-long range anti-ferromagnetic (AFM) correlations with a power-law decaying envelope as illustrated in Fig. 3.2(a). The correlations decay with an exponent of  $\eta \approx 1$  which puts the H-chain in the same universality class as the 1D Heisenberg model for large  $R$ . In addition to the AFM order,

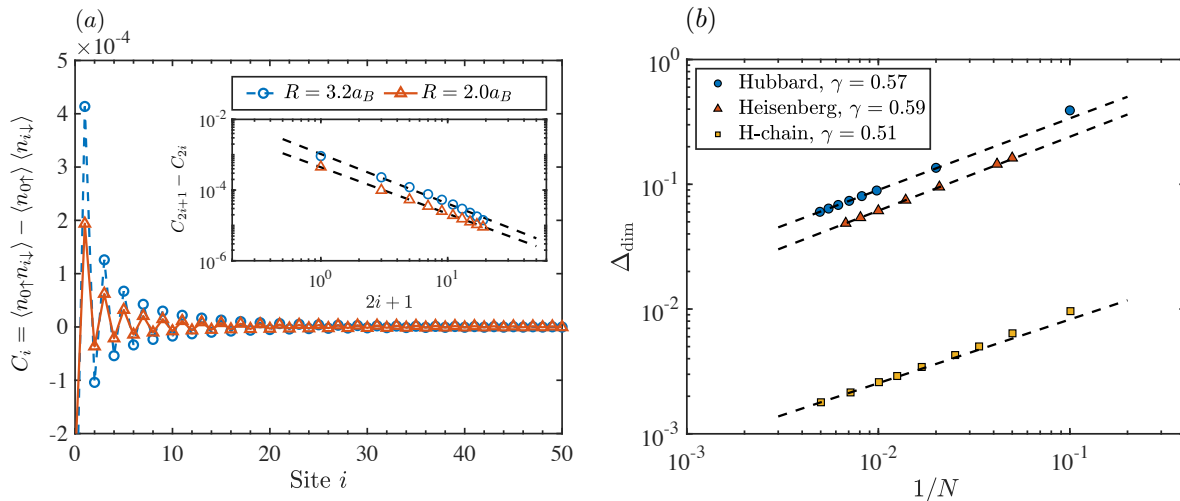


Figure 3.2: Ground state properties of the H-chain. (a) The anti-ferromagnetic correlations in H60 for  $R = 2.0a_B$  and  $R = 3.2a_B$ . The inset shows a power law decaying envelope for the correlations. (b) The dimerization in various lattice models as compared with the H-chain. For the Hubbard model, the dimerization is defined as  $\Delta_{\text{dim}} = \left| \left( \hat{c}_{N/2}^\dagger \hat{c}_{N/2+1} + h.c. \right) - \left( \hat{c}_{N/2+1}^\dagger \hat{c}_{N/2+2} + h.c. \right) \right|$ . For the Heisenberg model, it is defined as  $\Delta_{\text{dim}} = \left| \hat{S}_{N/2} \hat{S}_{N/2+1} - \hat{S}_{N/2+1} \hat{S}_{N/2+2} \right|$ . And for the H-chain, it is defined as the difference in the density between two adjacent bonds connecting the  $N/2$  and  $N/2 + 1$  hydrogen atoms.

the electron density shows signs of increasing dimerization as  $R$  is reduced. This is most apparent by comparing the electron density between even and odd bonds separating the nuclei. It can also be seen in the entanglement with an alternating pattern of low and high entropy along the chain as shown in Fig. 3.4. As the system size increases, this dimerization decreases as a power law, falling with an exponent  $d \approx 0.5$ . This behavior is reminiscent of the nearest neighbor spin correlations,  $\langle S_i S_{i+1} \rangle$  in the Heisenberg model and similarly the kinetic energy,  $h_i = \langle c_i^\dagger c_{i+1} + h.c. \rangle$  in the Hubbard model as shown in Fig. 3.2(b).

In the opposite limit, there exists some critical atomic spacing  $R_c < 1.8a_B$  for which the previously dormant bands beyond the  $1s$  become more occupied, transitioning the system from an insulating phase to a more metallic one. These additional bands are diffuse, emerging from the  $2s$ ,  $2p_x$ , and  $2p_y$  atomic orbitals and become occupied through a self-doping mechanism that drives the  $1s$  band occupancy below half-filling. We can see this by inspecting

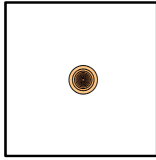
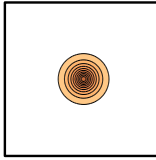
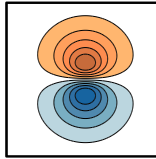
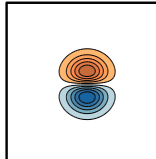
$R = 0.9a_B$			$R = 3.3a_B$		
	Orbital Type	Occupancy		Orbital Type	Occupancy
$s$		91%	$s$		99.4%
$p$		9%	$p$		0.6%

Figure 3.3: Natural orbital occupancy calculated by diagonalizing the single-body correlation matrix for H10 at (a)  $R = 0.9a_B$  and (b)  $R = 3.3a_B$ . For small  $R$ , the system is metallic and shows non-zero occupancy in the diffuse  $p$  orbitals. On the opposite end, in the insulating phases, the occupancy is primarily dominated by compact  $s$ -type character.

the natural orbital occupancy shown in Fig. 3.3 for  $R = 0.9a_B$  and  $R = 3.3a_B$ , two points that are deep in the metallic and insulating phases, respectively. As a simple picture, we can imagine a set of isolated bands that exists at large  $R$ , where the bandwidths are small, gradually transitioning to larger bandwidths as  $R$  is decreased and the orbitals begin to overlap. With much larger bandwidths, part of the  $1s$  band rises above the Fermi level while the  $2s/2p$  bands begin to cross below the Fermi level, leaving partially occupied bands that show metallic behavior. However, this simple picture does not explain which of the diffuse orbitals plays a more significant role in facilitating the transition.

### 3.1.1 Nature of Metal-Insulator Transition

As previously mentioned, there are several key bands that govern the physics of the H-chain over a range of atomic spacings: the  $1s$ ,  $2s$ ,  $2p_x$ , and  $2p_y$  orbitals. Using sb-DMRG, we can investigate the properties of the many-body ground state by diagonalizing the single-particle

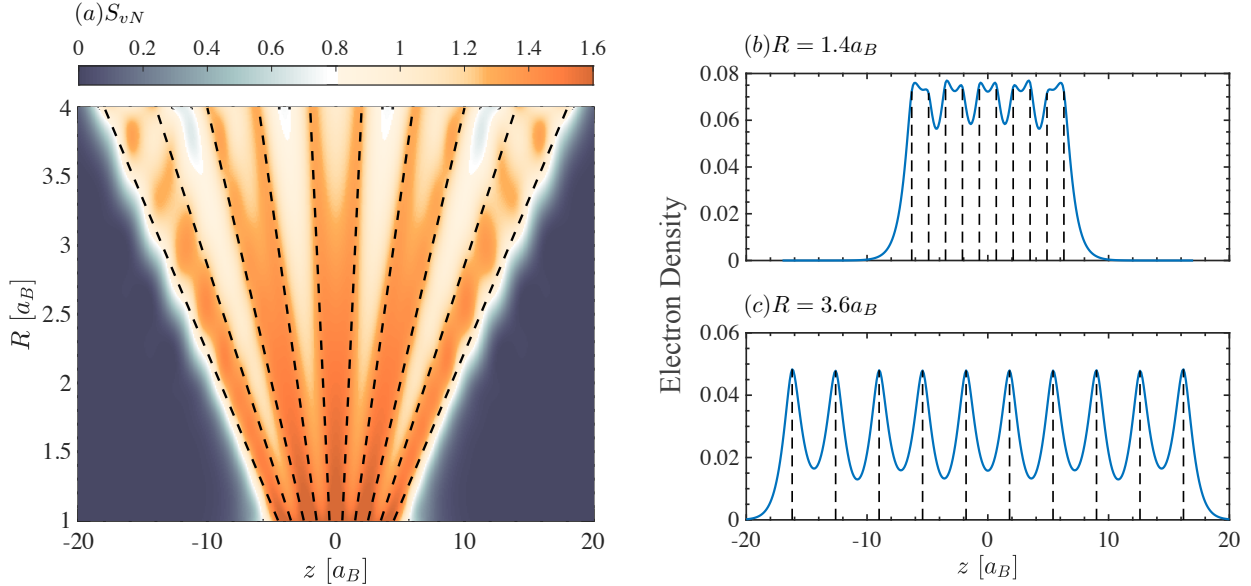


Figure 3.4: Ground state entanglement and density. (a) The von Neumann entanglement measured along the 1D chain for H10 at different values of atomic spacing. As  $R$  increases, the dimerization persists, but weakens. This is also seen by comparing the density and even and odd bonds as shown in the left column for (b)  $R = 1.4a_B$  and (c)  $R = 3.6a_B$ . In all plots, the dashed lines correspond to the positions of the nuclei.

density matrix for the full system or for a single slice and study the resulting natural orbitals and their corresponding occupancies. In order to avoid biases in the orbitals that become occupied, we choose to parameterize the H-chain with a diverse set of basis functions shown in Fig. 3.5.

Within the sliced-basis, the single-particle density matrix is expressed as

$$C_{ij}^{mn'} = \langle c_{ni,\uparrow}^\dagger c_{n'j,\uparrow} \rangle + \langle c_{ni,\downarrow}^\dagger c_{n'j,\downarrow} \rangle \quad (3.1)$$

where  $n, n'$  enumerate the slices and  $i, j$ , the local orbitals. Due to the orthogonality of the  $s$ ,  $p_x$  and  $p_y$  functions,  $C$  will be block diagonal, with three blocks representing the three types of functions. Furthermore, since the H-chain is symmetric under a rotation that takes  $x \rightarrow y$ , the  $p_x$  and  $p_y$  block will be identical. Therefore, we only consider the  $s$  block and the  $p_x$  block for the following analysis.

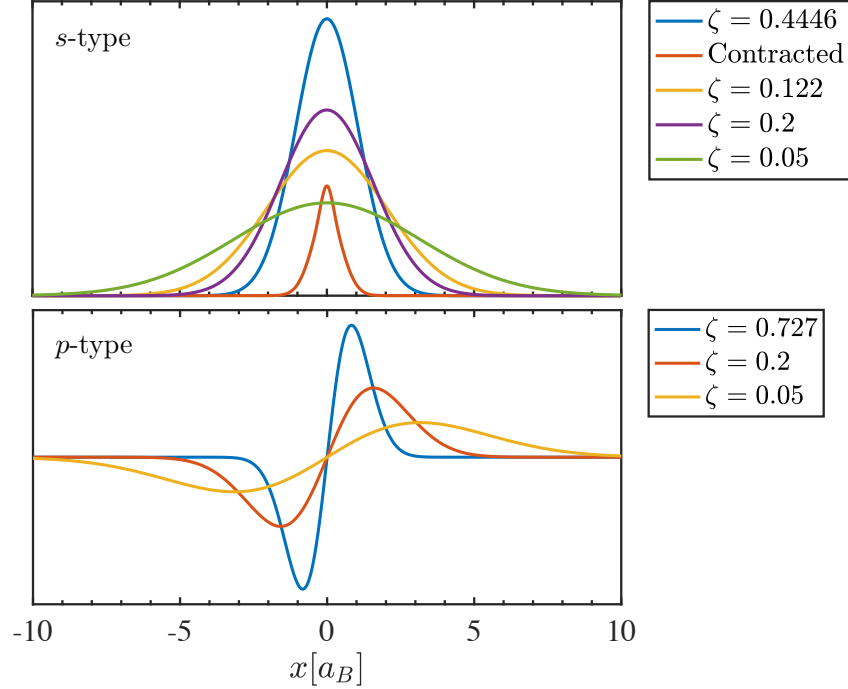


Figure 3.5: Gaussian basis that are used to make the sliced-basis functions. The  $s$ -type function labeled by “Contracted” is a contraction of the  $\zeta = 1.962$  and  $\zeta = 13.01$  Gaussians with coefficients 0.1379770 and 0.0196850, respectively. For the  $p$ -type functions, only the  $p_x$  are shown. The  $p_y$  functions are the same except they extend the  $y$ -axis instead of the  $x$ -axis.

To obtain a description of the many-body state at small and large  $R$ , we can diagonalize the  $s$  and  $p$  blocks of  $C$  separately and inspect the natural orbitals (NOs) with the highest occupancy. At half-filling, the diffuse  $2s$  and  $2p$  bands show only minor discrepancies, making it difficult to conclude which, if either, are favored. To make this difference more pronounced, we can study the occupancies of the equivalent electron-doped systems and track which band the extra electron occupies. These are shown in Fig. 3.6 for a metallic state at  $R = 1.3a_B$  and an insulating state at  $R = 1.8a_B$ . Comparing the occupancy of the diffuse orbitals between the two states, we see the extra electron goes into the  $2s$  band in the insulating state, but then transitions to the  $2p$  band as the system becomes metallic. This suggests that the two bands are competing, with one band being much more energetically favorable than the other depending on which side of the metal-to-insulator transition the system lies in. To resolve the energy differences we can employ a technique similar to what was done in section

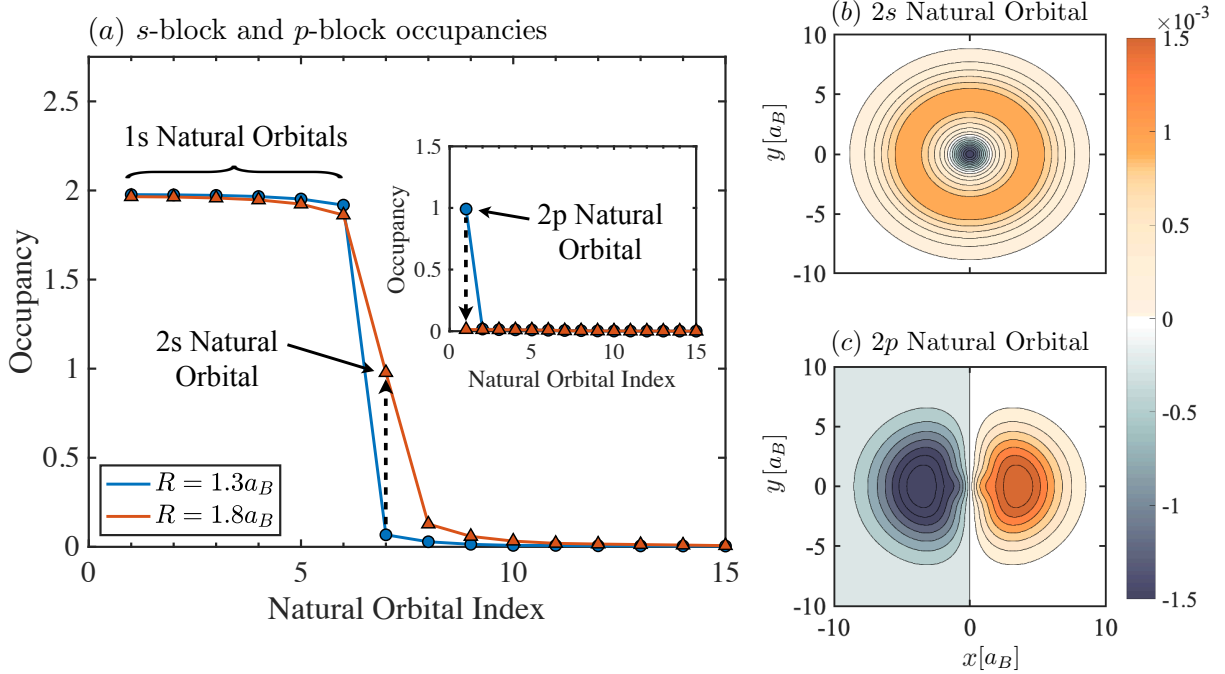


Figure 3.6: Natural Orbitals and their corresponding occupancies for the  $s$ - and  $p$ -blocks of the one-body correlation matrix. (a) As  $R$  is increased, we can see the extra electron moving from the  $2p$  NO to the  $2s$  NO. These orbitals are shown in (b) and (c). Note that the  $x$ - $y$  symmetry is broken here and the extra electron arbitrarily chooses to occupy  $2p_x$ . The symmetry is expected to be restored when the number of states kept tends to infinity.

2.2.1 and construct Fock operators for each of the NOs. These can then act on the vacuum to artificially create states in which the  $2s$  or  $2p$  band are occupied by the extra electron. By measuring the expectation value of the original Hamiltonian with respect to these states, we can probe the energy differences to see which band, if either, is most favorable.

Let's consider a 12 atom H-chain in the sliced basis defined by the functions in Fig. 3.5. To form the  $1s$  and  $2s$  Fock operators, we first diagonalize the  $s$  block of  $C$  from an electron-doped system and inspect the NO occupancy. The  $1s$  NOs are those that are close to doubly occupied while the  $2s$  NO is the one following immediately after the last  $1s$  NO (see Fig. 3.6). The same is done for the  $2p$  orbital, except in this case, we take the most highly occupied NO of the  $p_x$  block to represent the  $2p$  NO. Let  $\phi_{1s,j}^{ni}$  represent the  $j^{\text{th}}$   $1s$  NO and  $\phi_{2s}^{ni}$  and  $\phi_{2p}^{ni}$  represent the  $2s$  and  $2p$  NOs in the sliced basis where  $n$  enumerates the slice and  $i$ , the

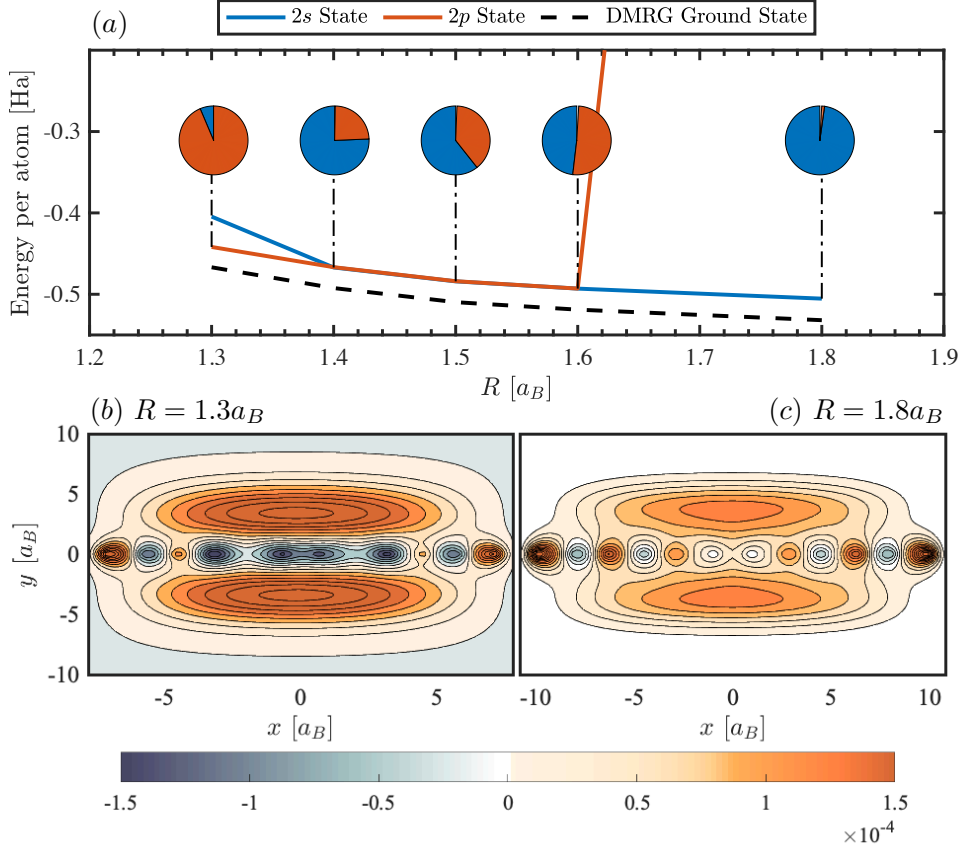


Figure 3.7: Energy differences in occupying  $2s$  versus  $2p$ . (a) The energies for the two states given in (3.3) and (3.4) as a function of  $R$ . The pie charts above each point indicate the  $2s$  and  $2p$  occupancy of the extra electron in the original system. The density relative to half-filling of the doped system is shown in (b) when the extra electron mostly occupies the  $2p$  NO and in (c), when it mostly occupies the  $2s$  NO.

local slice function. The corresponding Fock operators are given by

$$d_{\alpha}^{\dagger} = \sum_{ni} \phi_{\alpha}^{ni} c_{ni}^{\dagger}, \quad \alpha \in \{(1s, 1), (1s, 2), \dots, (1s, 6), 2s, 2p\} \quad (3.2)$$

The  $2s$  and  $2p$ -occupied states can then be written as

$$|\Psi\rangle_{2s} = d_{2s}^{\dagger} d_{1s,1}^{\dagger} d_{1s,2}^{\dagger} \dots d_{1s,6}^{\dagger} |0\rangle \quad (3.3)$$

$$|\Psi\rangle_{2p} = d_{2p}^{\dagger} d_{1s,1}^{\dagger} d_{1s,2}^{\dagger} \dots d_{1s,6}^{\dagger} |0\rangle \quad (3.4)$$



We can then take the expectation value of the original H-chain Hamiltonian with respect to these two states and compare the energies.  $\epsilon$  shows the energy difference between these two states as a function of  $R$  for H12. At large  $R$ , we can see that the  $2s$  band is much more energetically favorable, but becomes less favorable as  $R$  is decreased below the transition point. In addition, there is a striking asymmetry in the energy differences between  $2s$  and  $2p$  on either side of the transition, with the metallic side showing a much smaller energy difference than the insulating side. Around the transition point, the two bands seem to be degenerate over a small range of  $R$ , suggesting a tendency for the two bands to mix.

In addition to the energy and occupancy, we can visually inspect the electron density of the doped system relative to the half-filled system in order to determine where the extra electron has gone. From Fig. 3.7(b), we can see that the electron density has decreased in the bulk of the chain in favor for the more diffuse regions on the periphery. These regions are mainly of  $2p$  character as the previously shown. After the metal-to-insulator transition, the extra electron continues to occupy the more diffuse orbitals, but is more tightly bound to the chain. Looking in the bulk of the chain, we can also see a much more striking difference in the occupancy relative to the metallic H-chain.

# Chapter 4

## Deriving Effective Models for the Hydrogen Chain

Despite the prevalence of the downfolding techniques presented in chapter 1, it remains difficult to systematically verify the validity of these approaches. In the absence of experimental data, the systems which are being downfolded must be accurately simulated in order to compare quantities between the effective model and the original system. This was recognized by Shinaoka et al., who tested the accuracy of the widely employed cRPA technique when downfolding a three-band Hubbard model into a single-band effective model.[58] However, doing these checks for many real systems is impractical since modern many-body methods can not yet accurately simulate realistic materials. Instead, we can compare systems which exhibit relevant aspects of real materials, but are simple enough to remain accessible to modern many-body techniques. As we saw in the previous chapter, the hydrogen chain(H-chain) exhibits both of these aspects and is a promising candidate for studying the transition from a realistic material to an effective model.

Here we use results from sb-DMRG to construct effective models for the H-chain. The main

Function Type	Width
$s$ , contracted	$0.478(\zeta = 0.4446) + 0.138(\zeta = 1.962) + 0.020(\zeta = 13.01)$
$s$	$\zeta = 0.122$
$p_x$	$\zeta = 0.727$
$p_y$	$\zeta = 0.727$

Table 4.1: CC-pVDZ Basis Set. The contracted basis function shows the coefficient with the corresponding Gaussian width in parentheses.

approach will be to derive WFs for a set of relevant bands within the H-chain and transform to this new basis which defines our lattice model. From there, we can make various controlled approximations to truncate the downfolded model parameters to get even simpler models. At each step of the process, we can check the accuracy of the truncations. With access to the ground state and excited state wavefunctions to both the lattice model and the original system, we compare quantities such as the entanglement, correlations and spin velocities in order to probe the accuracy of different approximations used to construct the effective models. The comparisons will focus on the necessity of the long-range Coulomb interaction and beyond nearest-neighbor hopping in capturing the relevant physics of the H-chain.

## 4.1 Simulating the Hydrogen Chain

Within the sliced-basis, the full, 3D, H-chain Hamiltonian takes the form of a 1D multi-band model with long-range Coulomb interactions. We consider a system of  $N_a$  atoms separated at a distance  $R$  and placed on the  $z$ -axis, with the slices lying along the  $x$ - $y$  plane. In what follows, we choose the CC-pVDZ Gaussian basis set shown in Table 4.1 to span the slices and implement “hard wall” boundary condition as described in section 2.2.3. In this basis, the H-chain has two  $s$ -type functions and two  $p$ -type functions for a total of four functions per slice.

As noted in chapter 3, the H-chain begins to resemble the Hubbard model at large  $R$  and one

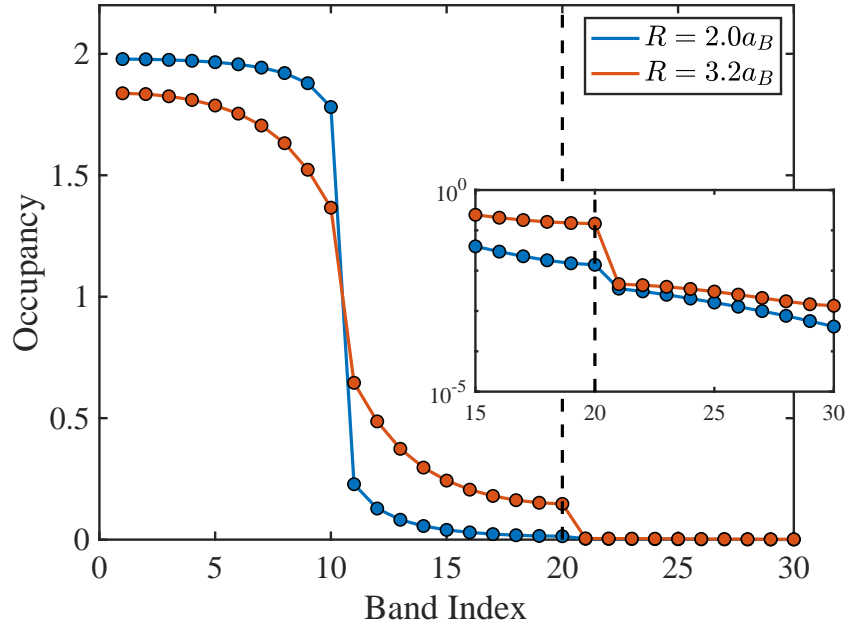


Figure 4.1: Eigenvalues of the single-particle correlation matrix from the ground state of H20 giving the natural orbital occupancy. The first 10 states are doubly occupied and represent Hartree-Fock type states. The second 10 states have small but non-negligible occupancy. States beyond the first 20 show occupancy on the order of  $10^{-3}$  and are truncated to give a downfolding approximation.

may imagine deriving a Hubbard-like effective model in this regime. Deep in the insulating phase, the more diffuse bands are significantly less occupied than the  $1s$  band which makes reducing to a single-band a good approximation. In addition to increasing the efficiency of the calculation, this will also facilitate the construction of a single-band effective model. Therefore we reduce the original four functions per slice down to a single slice natural orbital as described in section 2.2.2 resulting in a single-band description of the H-chain.

## 4.2 Wannier Functions for Interacting Systems

As described in section 1.1.2, Wannier functions(WF) are formed from single-particle states which result from tight-binding models, DFT calculations or other similar approximations. They are well defined in an independent-electron picture and are frequently used to construct

effective model Hamiltonians, which are then refined by other techniques(see chapter 1) to create an accurate representation of the original system. In addition to these traditional WFs, one can construct similar functions for fully interacting systems where the single-particle Bloch orbitals are no longer well defined.

As pointed out in [30], one can use the single-particle density matrix, which is well-defined even in an exact theory, as a surrogate for the Hamiltonian. One then takes its eigenstates(the natural orbitals), sorts them into bands according to their eigenvalues(the natural orbital occupancies) and constructs WFs. Of course, the full interactions fractionally populate the omitted bands and reducing to the WFs is an approximation. A good measure of the size of the error in going to the WF basis is in the total occupancy of all the omitted natural orbitals which we find to vary between  $10^{-3}$  to  $10^{-4}$  depending on  $R$ (see Fig. 4.1), making this a good approximation for the systems studied here.

This is the basic approach used here with sb-DMRG, but we can go even further and use eigenvectors of not just the ground state single-particle density matrix, but rather a sum of density matrices from a set of low-lying many-particle excited states in addition to the ground state, in order to capture information that describes the physics beyond the ground state. Generally, adding density matrices results in new eigenstates which attempt to cover the space of all the important states of the individual density matrices. We find that using this sum with a well-chosen set of excited states leads to a better representation of the low-energy physics in the downfolded model, such as the gaps between low-lying states. Choosing which low-lying states to incorporate into the sum of density matrices is key since too many incorporated states will lead to more truncation unless one uses a less simplified model. Too few may contribute to errors in reproducing the low-energy physics.

From (2.15), we can see that expressing the original 3D H-chain Hamiltonian in the sliced-basis has resulted in a 1D single-band lattice Hamiltonian. Reduced to 1D, we can now regard this system from a Luttinger Liquid perspective, for which all low-lying excitations

are bosonic spin and charge excitations. However, extra electrons added to the H-chain generally occupy additional bands which tend to be diffuse, as was shown in the previous chapter. A single-band effective model cannot properly capture such excitations, so we explicitly omit charge excitations from consideration in building our effective models—the charge excitations in the resulting models are expected to be qualitatively different from charge excitations of the H-chain. In contrast, the spin excitations do primarily live in the original single band. Therefore, in addition to the ground state density matrix, density matrices from states with one- and two-spinon pair excitations are added, i.e. total spin  $S_{\text{total}}^z \leq 2$ . Since the excitations only affect the spin-independent Wannier functions, we only create spin excitations in the spin- $z$  direction, speeding the calculations.

Specifically, the single-particle density matrix is calculated using the ground state  $|\Psi_0\rangle$ , 1-spinon pair excited state  $|\Psi_1\rangle$  and 2-spinon pair excited state  $|\Psi_2\rangle$  of the H-chain as

$$\begin{aligned}
C_{ij}^{(0)} &= \langle \Psi_0 | \hat{c}_{i\uparrow}^\dagger \hat{c}_{j\uparrow} + \hat{c}_{i\downarrow}^\dagger \hat{c}_{j\downarrow} | \Psi_0 \rangle \\
C_{ij}^{(1)} &= \langle \Psi_1 | \hat{c}_{i\uparrow}^\dagger \hat{c}_{j\uparrow} + \hat{c}_{i\downarrow}^\dagger \hat{c}_{j\downarrow} | \Psi_1 \rangle \\
C_{ij}^{(2)} &= \langle \Psi_2 | \hat{c}_{i\uparrow}^\dagger \hat{c}_{j\uparrow} + \hat{c}_{i\downarrow}^\dagger \hat{c}_{j\downarrow} | \Psi_2 \rangle
\end{aligned} \tag{4.1}$$

The mixed density matrix is then given by  $C_{ij} = C_{ij}^{(0)} + C_{ij}^{(1)} + C_{ij}^{(2)}$  and the natural orbitals,  $\{\xi_k\}$ , are readily obtained by diagonalization.

For an  $N_a$ -atom hydrogen chain, the  $N_a$  most occupied natural orbitals are retained whereas the rest are projected out. In the weakly correlated regime, the spectrum of the ground state density matrix exhibits a sharp cutoff between occupied and unoccupied states whereas in the strongly correlated regime, the spectrum is more flat, reflecting the tendency for these states to mix. However in both of these regimes, there exists a sharp cutoff between the first  $N_a$  states and the rest, as shown in Fig. 4.1. Spectra from density matrices of low-lying states (e.g. those generated by spinon excitations) also demonstrate the same feature,

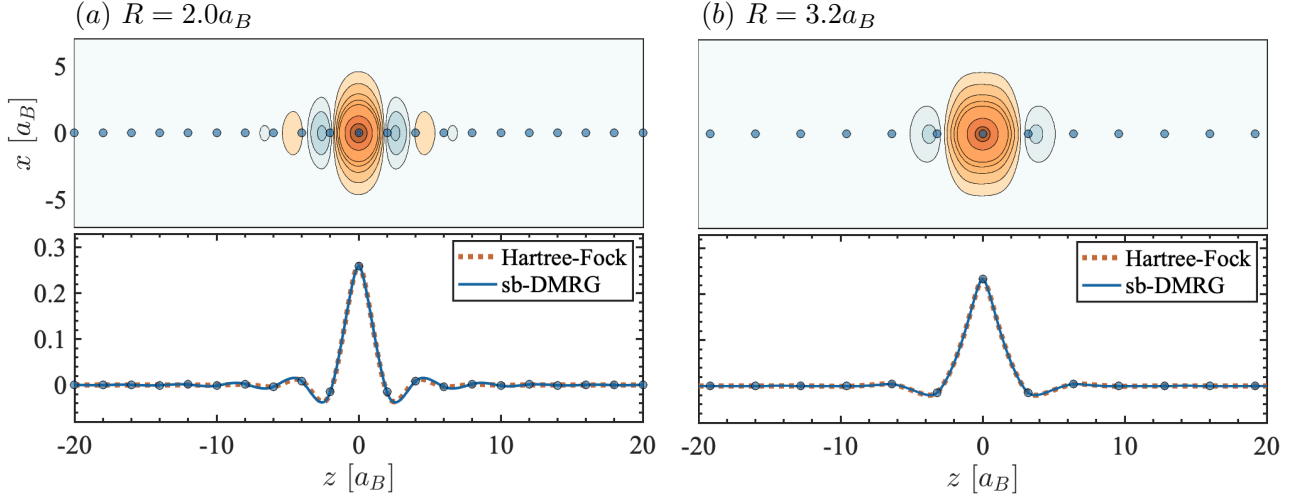


Figure 4.2: Translationally invariant Wannier function for (a)  $R = 2.0a_B$  and (b)  $R = 3.2a_B$  constructed from the single-particle density matrices of H100. The top panels in each subplot show the full 3D Wannier functions in real-space integrated over  $y$  and the lower panels, the 1D representation within the sliced basis as a function of  $z$  for both sb-DMRG and Hartree-Fock derived functions.

indicating that the ground state and a group of low-lying excited states are confined to the states below this cutoff. Therefore by diagonalizing a mixture of density matrices, information regarding excited states can be captured explicitly and used to construct the effective model. The  $N_a$  remaining natural orbitals are then localized around each atom by projecting the 1D position operator into this basis and re-diagonalizing. This is exactly analogous to the spread minimization procedure used in the construction of maximally localized WFs discussed in section 1.1.2.

The procedure described thus far yields slightly different WFs describing each atom. This is a consequence of using open boundary conditions and as such, only the WFs near the edge differ much from those in the bulk. In order to better reproduce the model in the thermodynamic limit, we restore translational invariance among the WFs by first aligning them so that all the maxima coincide at one point, then average point-wise across all functions, weighing each function by their proximity to the center of the chain. The translationally invariant WF shown in Fig. 4.2 is then redistributed to each atom.

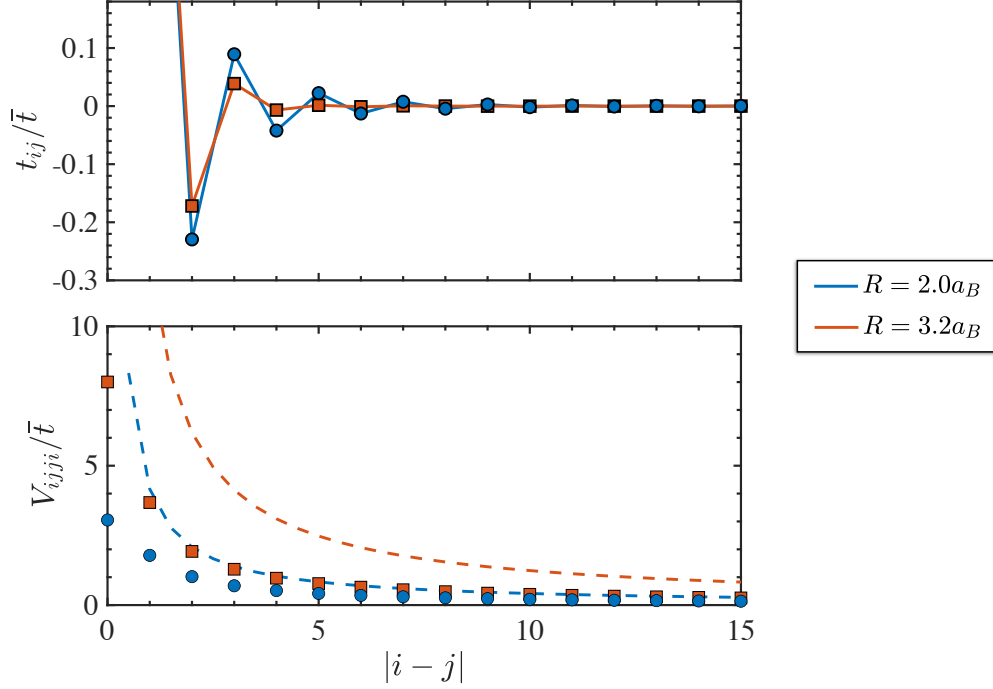


Figure 4.3: Hamiltonian parameters from transforming the H-chain Hamiltonian into an effective model using the Wannier functions for H100. All parameters are scaled by the average value of the nearest neighbor hopping denoted by  $\bar{t}$ . The top panel shows the single-body terms and the lower panel, the two-body interaction terms. The dashed lines in the lower panel are  $1/r$  lines in units of  $\bar{t}$ .

The WFs are defined by the coefficients  $w_{ni}$ , where  $n = 1, 2, \dots, N_z$  enumerates the grid and  $i = 1, 2, \dots, N_a$ , the functions. The Hamiltonian then takes the form

$$\hat{H}_{\text{WF}} = \sum_{\sigma, ij} t_{ij}^{\text{WF}} \hat{c}_{\sigma i}^{\dagger} \hat{c}_{\sigma j} + \frac{1}{2} \sum_{\sigma, ijkl} V_{ijkl}^{\text{WF}} \hat{c}_{\sigma i}^{\dagger} \hat{c}_{\sigma' j}^{\dagger} \hat{c}_{\sigma' k} \hat{c}_{\sigma l}$$

$$t_{ij}^{\text{WF}} = \sum_{nn'} w_{in}^* t_{nn'}^{\text{sb}} w_{n'j} \quad (4.2)$$

$$V_{ijkl}^{\text{WF}} = \sum_{nn'} w_{in}^* w_{jn'}^* V_{nn'}^{\text{sb}} w_{kn'} w_{ln}.$$

The resulting Hamiltonian parameters are shown in Fig. 4.3.

As previously mentioned, in typical applications, Wannier functions are constructed from single-particle orbitals of mean-field calculations, so it is natural to compare the performance



of such functions to those obtained from sb-DMRG. Although density functional approaches may be better, for simplicity we compare unrestricted Hartree-Fock in place of sb-DMRG to construct these functions and as Fig. 4.2 indicates, we find very similar Wannier functions. In this case, we see that a conventional Wannier construction would likely be satisfactory, although we expect higher accuracy from our sb-DMRG approach.

### 4.3 Variational Optimization of Effective Models

The Hamiltonian in (4.2) is the most general lattice model containing up to two-body terms. It is therefore desirable to truncate the tensors  $\{t_{ij}^{WF}\}$  and  $\{V_{ijkl}^{WF}\}$  in order to recover a Hubbard-like model or models with density-density interactions. For systems at finite temperatures, one can search for an effective model such that the canonical density operator for the model closely approximates that of the original system. This leads to a minimization procedure involving the Peierls-Feynman-Bogoliubov variational principle, resulting in an effective model.[56]

At zero temperature, this procedure translates into minimizing the expectation value of the original Hamiltonian with respect to the ground state of a trial effective model. As deviations from the true ground state occur, one can vary the parameters in the effective model until the expectation value closely approximates the ground state energy of the original system. In the best case scenario, the effective model will yield a wavefunction that is nearly identical to that of the original system. Furthermore, if a small manifold of low energy states near the ground state also match between the two systems, then the resulting effective model would be an excellent representation of the original system.

Let's take (4.2) to be our starting Hamiltonian. We would like to find a simpler effective

model of the form

$$\hat{H}_{\text{eff}} = \sum_{ij} t_{ij} \hat{c}_{\sigma i}^\dagger \hat{c}_{\sigma j} + \frac{1}{2} \sum_{ij} V_{ij} \hat{n}_i \hat{n}_j \quad (4.3)$$

where  $\{t_{ij}\}$  and  $\{V_{ij}\}$  are band-diagonal such that all elements with indices  $|i - j| > l_t$  and  $|i - j| > l_V$  are zero, respectively. Note here that the original four-index interaction has been replaced by a much simpler two-index, density-density interaction. Working at zero temperature, the Peierls-Feynman-Bogoliubov variational principle reduces to a minimization of

$$\Phi[t_{ij}, V_{ij}] = \langle \Psi_{\text{eff}} | \hat{H}_{\text{WF}} | \Psi_{\text{eff}} \rangle \quad (4.4)$$

with respect to the model parameters  $\{t_{ij}\}$  and  $\{V_{ijkl}\}$ . Here,  $|\Psi_{\text{eff}}\rangle = |\Psi_{\text{eff}}[t_{ij}, V_{ij}]\rangle$  is the ground state of  $\hat{H}_{\text{eff}}$  and is a complicated function of  $\{t_{ij}\}$  and  $\{V_{ijkl}\}$ . This procedure is used in [56] for the case of reducing long range two-particle interactions to an on-site interaction. For this case, the form of the optimal on-site interaction can be explicitly found and solved self-consistently. Here the method has been generalized to adjust all of the one-particle terms and all of the two-particle terms which yields a system of equations that need to be solved self-consistently. As the number of equations increase, solving them to find the optimal parameters quickly becomes unstable. Instead, we directly vary the parameters of  $\hat{H}_{\text{eff}}$  and use iterative algorithms to find the minimum.

At each step of the optimization, the function evaluation is carried out by first defining a Hamiltonian according to the variational parameters  $t_{ij}$  and  $V_{ij}$  and then solving for the ground state using DMRG, yielding  $|\Psi_{\text{eff}}\rangle$ . Then (4.4) can be used to evaluate  $\Phi[t_{ij}, V_{ij}]$  by taking the energy overlap with respect to this wavefunction. The number of sweeps for each DMRG run is very small—usually no more than one or two—since the wavefunction from the previous step can be used as a starting point for the DMRG at the current step. This

is sufficient for optimization algorithms such as Nelder-Mead which use a simplex defined in parameter space to gradually reach a minimum since function evaluations are all that is required.

For the family of optimization algorithms that take advantage of the local gradients (e.g. Gradient/Conjugate Gradient Descent and the Broyden-Fletcher-Goldfarb-Shanno (BFGS) algorithm), the ability to differentiate (4.4) is an additional, but worthwhile requirement. Exactly computing the gradients is impractical since the wavefunction used to calculate the expectation value is some complicated function of the model parameters. So in order to use any gradient dependent algorithm, the derivatives must be approximated.

For simplicity, let's consider the case in which our effective Hamiltonian takes the form

$$\hat{H}_{\text{eff}} = \sum_{\langle ij \rangle} (\hat{c}_{\sigma i}^\dagger \hat{c}_{\sigma j} \text{ h.c.}) + U \sum_i \hat{n}_{i\uparrow} \hat{n}_{i\downarrow} + V_1 \sum_i \hat{n}_i \hat{n}_{i+1} + V_2 \sum_i \hat{n}_i \hat{n}_{i+2} \quad (4.5)$$

where the summation over spins is implied and we have re-scaled the energy such that  $t = 1$ . As an approximation, we can use finite differences to calculate the gradients. We pick some small parameter  $\epsilon$  and compute the gradients as

$$\begin{aligned} \partial_U \Phi &\approx \frac{\Phi[U + \epsilon] - \Phi[U]}{\epsilon} \\ \partial_{V_1} \Phi &\approx \frac{\Phi[V_1 + \epsilon] - \Phi[V_1]}{\epsilon} \\ \partial_{V_2} \Phi &\approx \frac{\Phi[V_2 + \epsilon] - \Phi[V_2]}{\epsilon} \end{aligned} \quad (4.6)$$

In each of the function evaluations involving a shift by  $\epsilon$  of the model parameter, a new wavefunction needs to be computed. However, just as in the case of the gradient-free algorithms, the previous wavefunction may be recycled, meaning that only a few DMRG sweeps are needed in order to get the new state. For the example shown above, the number of sweeps needed for all the function evaluations and gradients used in a single iteration is

$(2 * 3) + 2 = 8$ , two sweeps for each of the three variables to get the gradients plus an additional two sweeps for the function evaluation at the new set of parameters.

Note that the cost of calculating the gradients scales linearly with the number of model parameters. For effective models with long-range two-body interactions, this could potentially cause the number of sweeps per iteration to scale quadratically in the system size. But a more realistic two-body interaction, such as the Coulomb interaction, only requires a fraction of the variables since the interaction will be translationally invariant. With open boundary conditions, this is slightly relaxed to include variations in the parameters near the edge, but can still yield a number of parameters that is independent of the system size. The question then is how to define the “bulk” versus the “edge” region for these systems.

Suppose that a system for which we seek an effective model has interaction terms  $\{V_{ij}\}$ . For example, this may be a result of taking  $V_{ij} \equiv V_{ijji}^{\text{WF}}$  for the transformed H-chain interactions in (4.2). Let’s consider the diagonal elements of  $\{V_{ij}\}$  and denote them as  $\{U_i \equiv V_{ii}\}$  for  $i \in [1, N]$ . The “bulk” and “edge” parameters are chosen by separating a select number of sites near the edge from the remaining sites near the center. For an edge length of  $n$ , the “edge” parameters are defined as the first  $n$  and the last  $n$  elements in  $\{U_i\}$  which we write as  $\{U_i\}_{1:n,(N-n):N}$ . Similarly, the “bulk” parameters are defined as the middle  $N - 2n$  elements written as  $\{U_i\}_{n:(N-n)}$ . Then, we can compute the variance of the “bulk” elements and choose  $n$  such that this variance is below a particular threshold. Formally, we choose  $n$  when

$$\text{var} (\{U_i\}_{n:(N-n)}) \leq \lambda \tag{4.7}$$

is satisfied for a given value of  $\lambda$ . This procedure is then repeated for each diagonal band of  $\{V_{ij}\}$  to define separate bulk and edge regions. The parameters in the bulk region can be represented by a single variable while those in the edges are allowed to differ amongst

themselves. As an example, if we choose  $l_V = 2$  for the interactions in (4.3), the matrix will have the form

$$V = \begin{pmatrix} v_1 & v_4 & v_6 & 0 & \cdots & 0 & 0 & 0 & 0 \\ v_4 & v_2 & v_5 & v_6 & \cdots & 0 & 0 & 0 & 0 \\ v_6 & v_5 & v_3 & v_5 & \cdots & 0 & 0 & 0 & 0 \\ 0 & v_6 & v_5 & v_3 & \cdots & 0 & 0 & 0 & 0 \\ \vdots & \vdots & \vdots & \vdots & \ddots & \vdots & \vdots & \vdots & \vdots \\ 0 & 0 & 0 & 0 & \cdots & v_3 & v_5 & v_6 & 0 \\ 0 & 0 & 0 & 0 & \cdots & v_5 & v_3 & v_5 & v_6 \\ 0 & 0 & 0 & 0 & \cdots & v_6 & v_5 & v_2 & v_4 \\ 0 & 0 & 0 & 0 & \cdots & 0 & v_6 & v_4 & v_1 \end{pmatrix} \quad (4.8)$$

which has six variational model parameters,  $v_1 \dots v_6$ . This can also be done for the one-body terms, but with careful consideration of the diagonal elements (see appendix A.1).

Once the model parameters have been defined, we may implement the minimization of (4.4) using any gradient-required or gradient-free optimization algorithm as described above. In some cases, we found that this optimization could get stuck. As a simple fix, instead of optimizing all the parameters at once, we first optimize over the elements of  $V$ , keeping  $t$  fixed, then over the elements of  $t$ , keeping  $V$  fixed, then over  $V$  again, etc.

### 4.3.1 From Long-Range Interactions to On-site $U$

A simple test of the outlined optimization procedure is to reduce a Hubbard model with long-range Coulomb interactions into an effective model with only an on-site two-body term. Because the effective model has only one parameter, we can find the most optimal solution by searching the DMRG ground states of effective models with different on-site interactions

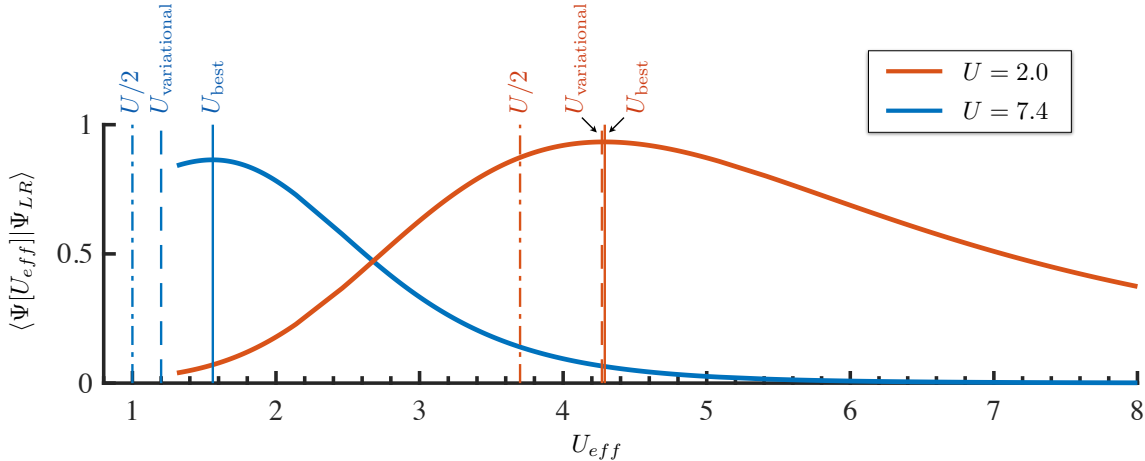


Figure 4.4: Comparison of the variational algorithm and a brute force search. The solid red and blue curves give the value of the ground state overlap between the long-range model (with  $U = 2.0$  in blue and  $U = 7.4$  in red) and the Hubbard model evaluated on a fine grid. The various vertical lines show the values of  $U_{\text{eff}}$  that correspond to the naive effective model with  $U_{\text{eff}} = U/2$ , the model found variationally and the best possible model.

defined on a 1D grid (as opposed to  $m$  variables which would require a search over an  $m$ -dimensional grid, an exponentially larger set of models than in the 1D case). Given the simplicity of simulating 1D Hubbard models in DMRG, we can quickly generate ground states for up to one hundred different models. Then for each ground state, we can compute the wavefunction overlap with the ground state from the original long-range model and choose an effective model by finding the one that maximizes this overlap. To compare how well the effective model from the optimization procedure fares against the one chosen by a brute force search, we simply compare the values of the on-site interaction. If the values closely match, the optimization procedure has successfully found a good effective model. If not, the optimization became stuck in a local minimum and could not reach an optimal solution.

Let's take the starting Hamiltonian to be

$$\hat{H}_{\text{LR}} = - \sum_{\langle ij \rangle} (\hat{c}_i^\dagger \hat{c}_j + h.c.) + U \sum_i \hat{n}_{i,\uparrow} \hat{n}_{i,\downarrow} + \sum_{i>j} V_{ij} \hat{n}_i \hat{n}_j, \quad V_{ij} = \frac{U/2}{|i-j|} \quad (4.9)$$

where the summation over spin is implied and the overall energy scale has been chosen such that  $t = 1$ . We would like to find an effective model that eliminates the last term in (4.9) and renormalizes the on-site  $U$  to a new value  $U_{\text{eff}}$  such that the new model reads

$$\hat{H}_{\text{eff}} = - \sum_{\langle ij \rangle} \left( \hat{c}_i^\dagger \hat{c}_j + h.c. \right) + U_{\text{eff}} \sum_i \hat{n}_{i,\uparrow} \hat{n}_{i,\downarrow}. \quad (4.10)$$

A brute force search over the model space is conducted by varying  $U_{\text{eff}}$  on a fine grid with spacing  $\Delta U = 0.1$  and using DMRG to find the corresponding ground states. Then for each state  $\alpha$ , we can compute  $\langle \Psi_{\text{eff}} | \Psi_{\text{LR}} \rangle_\alpha$  to find the model that maximizes the overlap. At the same time, we use the optimization procedure of the previous section to find a value of  $U_{\text{eff}}$  that minimizes (4.4) so that we may compare the two values. Here, the optimization is run with the BFGS algorithm which requires the gradient.

The results of these comparisons are shown in Fig. 4.4 for two different values of  $U$  used in the original model. For reference, we also plot the value of  $U/2 = U - V_{12}$ , a good first guess for the effective on-site interaction (choosing this value will lead to the same energy difference in both the original and effective models when a particle hops from one site to an adjacent site). [56] Given large values of  $U$ , the optimization procedure yields roughly the same effective model as the most optimal one recovered from a brute force search. We can also see that the value of  $U_{\text{eff}}$  is slightly larger than that given by  $U/2$ , meaning that higher order corrections involving particle fluctuations beyond nearest-neighbor contribute to the renormalization of  $U$ . For smaller values of  $U$ , we see that the optimization improves upon the initial guess of  $U/2$ , but struggles to find the optimal solution.

With smaller values of  $U$ , the corresponding states begin to show a high amount of entanglement and therefore makes it harder for a low-entanglement method such as DMRG to efficiently represent the state. In this regime, a small truncation error requires large bond dimensions, but is necessary in order to calculate the gradients (which are done using finite

differences) to a sufficient degree of accuracy. When the error in the energy becomes comparable to the size of the shift used to approximate the gradient, the efficiency of algorithms such as BFGS begin to break down and it becomes more difficult to approach the true minimum. One may then try a gradient-free algorithm, such as Nelder-Mead, but this requires many more function calls. Together with the need for a larger bond dimension, each iteration of the optimization procedure can become very slow.

Although this seems like a major drawback, it must be noted that these problems occur in a regime where the systems exhibit weaker correlations. For most applications of this optimization procedure, we are interested in downfolding a strongly correlated system into another strongly correlated effective model for which DMRG can be efficiently used. If an effective model is needed for a weakly correlated system, then one can apply the methods outlined in chapter 1. Therefore the overall downfolding strategy would be to employ a DFT-based method for weakly correlated systems, but transition into using this DMRG-based approach for more strongly correlated systems.

## 4.4 H-Chain Effective Models

One fundamental question regarding effective models is the necessity of the various terms that make up the Hamiltonian such as the next-nearest neighbor hopping, third-nearest neighbor hopping and the range of the Coulomb interaction. Given the method outlined in the previous section, we can apply it to a host of effective models, each with a different set of single-particle and two-particle terms. Then by comparing each of the resulting models to the original, we can gauge the importance of the hopping and the two-body interactions, specifically their relative magnitudes and range.

In what follows, we first establish a baseline effective model using (4.2), which includes the



full-range hopping and two-particle interactions. We can then restrict the range of each of these terms, and optimize over the remaining terms. Finally, we can reduce the effective model to a pure Hubbard model defined by an optimal hopping,  $t$  and optimal on-site interaction  $U$ .

#### 4.4.1 Truncating the Four-Index Interactions

The presence of four-index terms,  $V_{ijkl}^{\text{WF}}$ , greatly increases the MPO bond dimension, strongly restricting the length of the chains we could study. Inspecting the four-index terms, we find that the majority of elements with  $i \neq l$  and  $j \neq k$  are small, on the order of  $10^{-6}$  –  $10^{-5}$ , indicating a truncation of these terms may have negligible effects on the final model. Therefore in order to treat much larger system sizes, we first reduce to an intermediate model, keeping the hopping fixed, but reducing  $V_{ijkl}^{\text{WF}}$  to the diagonal  $V_{ij}$  form shown in Eq. (4.3), without restricting the range of the interactions. The diagonal form is approximated from the four-index terms as  $V_{ij} \approx V_{ijji}^{\text{WF}}$ . To establish that this is a good approximation, we first assume

$$V_{ij} = V_{ijji}^{\text{WF}} + \delta_{ij}\epsilon_i \quad (4.11)$$

and perform the optimization described in the previous chapter over the set  $\{\epsilon_i\}$  on medium length chains, up to  $N_a = 20$  atoms. On such systems, the corrections turn out to be quite small,  $\{\epsilon_i\} \sim 10^{-2}$ . When comparing the ground states energies and wavefunctions between the original system and its diagonal approximation, we find errors on the order of  $10^{-3}$  for both the energy difference and wavefunction overlap, indicating that the truncation of these terms is justifiable. Under this approximation, the Hamiltonian becomes,

$$\hat{H}_{WF} = \sum_{\sigma, ij} t_{ij}^{\text{WF}} \hat{c}_{\sigma i}^\dagger \hat{c}_{\sigma j} + \frac{1}{2} \sum_{\sigma, ij} V_{ijji}^{\text{WF}} \hat{n}_{\sigma i} \hat{n}_{\sigma' j} \quad (4.12)$$

We will use this approximation for  $\hat{H}_{WF}$  for the remaining sections of this chapter.

#### 4.4.2 Long-Range Effective Models

A natural baseline can be established by taking the effective model to be  $\hat{H}_{WF}$ . This is the Hamiltonian that resulted from directly transforming the H-chain Hamiltonian with the WFs and subsequently replacing  $V_{ijkl}^{WF} \rightarrow V_{ij}$  as was done in Eq. (4.12). The accuracy of this and other effective models can be tested by comparing several quantities such as the spin velocity, single-particle Green's function and spin-spin correlation to those of the original H-chain. These are meant to quantify both the ground state properties as well as properties of the low-lying excited states. Since at this stage, no Hamiltonian parameters have been optimized, any errors in  $\hat{H}_{WF}$  can only result from either the truncation of the natural orbitals or the truncation of  $V_{ijkl}^{WF}$ .

The spin velocity is derived by measuring how the energy gap between the ground state and a spin-excited state scales with system size. This can be done for 1 and 2 pairs of spinons to get information on how well the effective model reproduces the low-energy physics of the original system. This is shown in Fig. 4.5 for several effective models as well as the original H-chain. For smaller systems of 20 and 40 atoms, the finite size effects can cause large errors in the gaps, both at  $R = 2.0a_B$  and  $R = 3.2a_B$ . At larger system sizes, these effects become much more negligible and it can clearly be seen that the gaps of the effective models begin to closely approximate the gaps in the original H-chain. Comparing the actual spin velocities, we find differences less than 10% between the H-chain and  $\hat{H}_{WF}$ .

In addition to the spin velocity, the single-particle correlations can be computed and compared across models. These are defined here as

$$g_i = \langle \hat{c}_{N/2\uparrow}^\dagger \hat{c}_{i\uparrow} + \hat{c}_{N/2\downarrow}^\dagger \hat{c}_{i\downarrow} \rangle \quad (4.13)$$

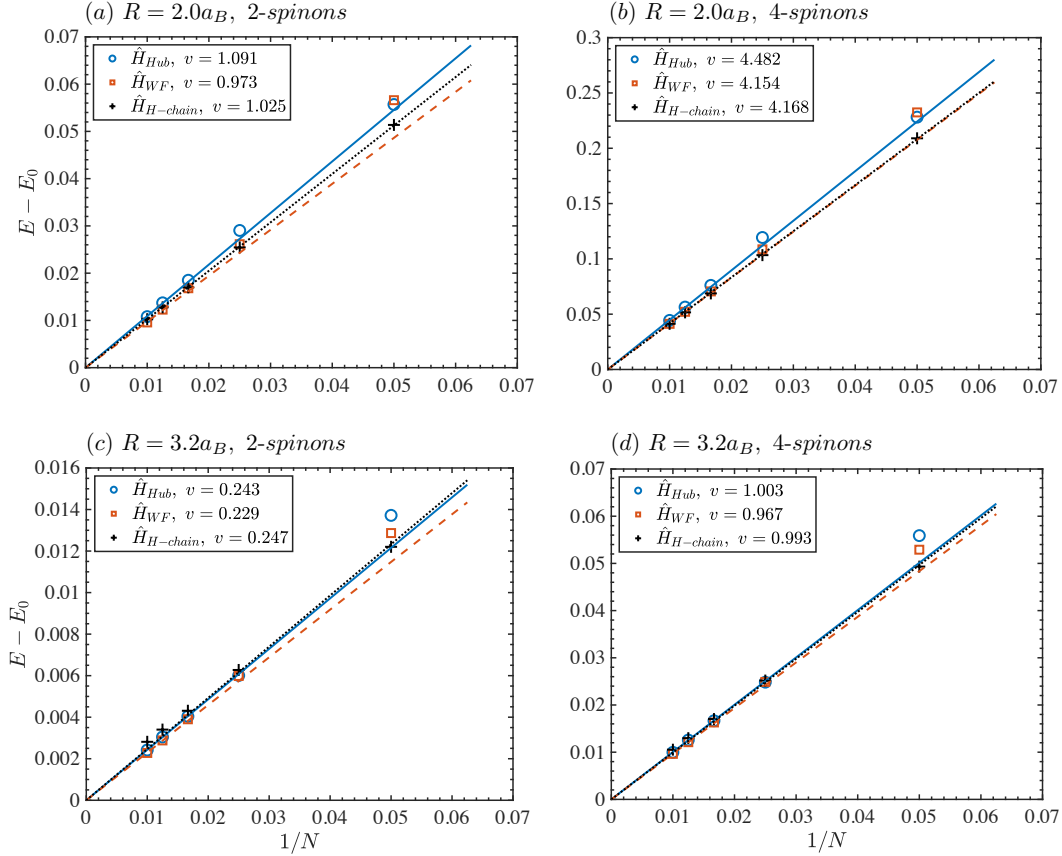


Figure 4.5: Spin velocities for the H-chain and two effective models defined in (4.12) and (4.15). The top row shows (a) 2-spinon and (b) 4-spinon excitation gaps at  $R = 2.0a_B$  for the H-chain, its corresponding directly transformed model denoted as  $\hat{H}_{WF}$  and optimal Hubbard model,  $\hat{H}_{Hub}$ . The same is done at  $R = 3.2a_B$  in the lower row for the (c) 2-spinon and (d) 4-spinon excitations. The numbers in the legend correspond to the slope of the fitted lines which give the spin velocities.

and are expected to decay as a power law (up to log corrections) for gapless systems, but exponentially in the presence of a gap. In the family of effective models tested here, the correlations are expected to decay exponentially since the charge sector is gapped. The single-particle correlations are shown in Fig. 4.6. In order to compare the correlations defined in the sliced-basis for the H-chain with those for the effective model (expressed in the space of atomic sites), we transform the single-particle Green's function of the original system using the WFs of the corresponding effective model. Measuring the correlation length in this space gives  $l_{H-chain} = 12.8$  and  $l_{WF} = 13.8$  for  $R = 2.0a_B$ , decreasing to  $l_{H-chain} = 3.4$

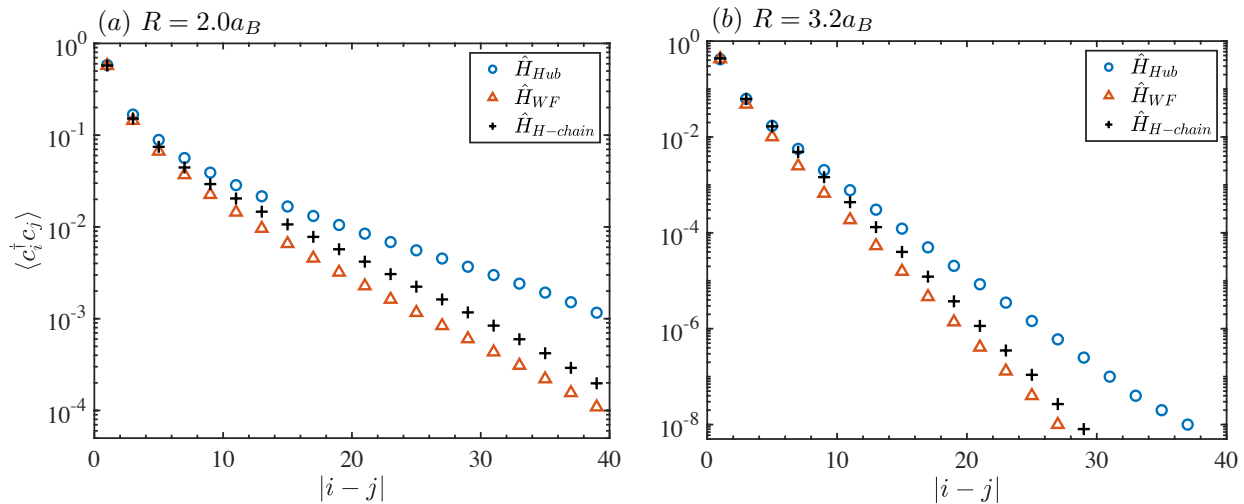


Figure 4.6: Single-particle correlations for the H-chain, its corresponding directly transformed model defined in (4.12) and optimal Hubbard model defined in (4.15) for H100 at (a)  $R = 2.0a_B$  and (b)  $R = 3.2a_B$ . The correlators are calculated from the middle of the chain to the right edge as defined in (4.13). Note here that, the WFs are used to transform the H-chain correlation functions into the same space as the effective models.

and  $l_{WF} = 3.7$  for  $R = 3.2a_B$ , corresponding to differences of about 8% between the H-chain and  $\hat{H}_{WF}$  for both atomic spacings. The spin-spin correlations can also be computed and are shown in Fig. 4.7.

The excellent agreement of both the correlations and spin velocities between  $\hat{H}_{WF}$  and the H-chain demonstrates the accuracy of the procedure used in deriving the WFs and the following truncation of the 4-index interaction terms. At this stage,  $\hat{H}_{WF}$  constitutes the initial set of interactions needed in order to accurately represent the H-chain. However, one can go further and deduce the minimum set of interactions needed to describe the original system with a certain accuracy.

### 4.4.3 Reducing the Range of the Interactions

Despite the existence of the full, long-range Coulomb interaction in the original system, can we reconstruct the ground state and spin excitations with shorter-range one-body and two-

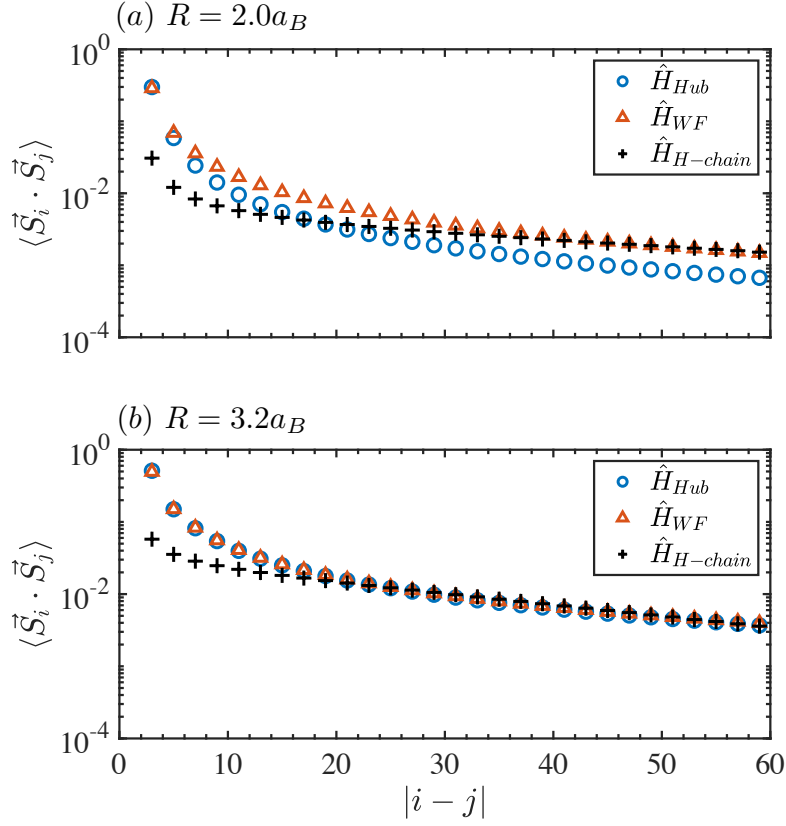


Figure 4.7: Spin-spin correlations at (a)  $R = 2.0a_B$  and (b)  $R = 3.2a_B$  for the original H-chain and its corresponding effective models defined in (4.12) and (4.15). The correlators are calculated from the left-most edge of the chain to the midpoint for a system of 100 atoms. The H-chain correlations have been scaled such that the point at site 50 match that of  $\hat{H}_{WF}$ .

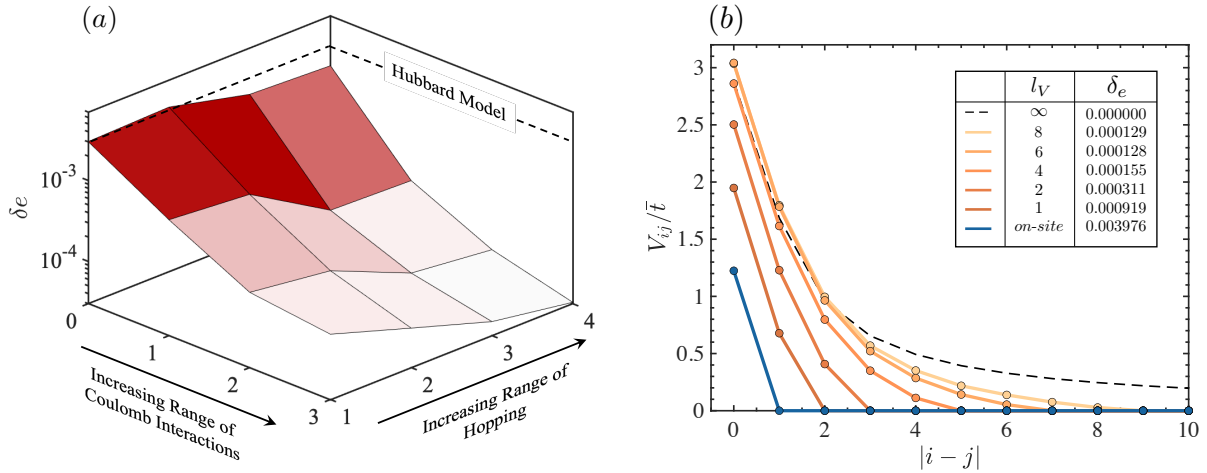


Figure 4.8: (a) Error for effective models with varying-range one-body and two-body interactions for H20 at  $R = 2.0a_B$ . The dashed black lines correspond to the error made by using only Hubbard interactions in the effective model as in (4.15). Increasing the range of the two-body interactions is seen to be more effective than increasing the range of the one-body hopping. (b) Decay of two-body interactions with varying maximum range for H40. The variable  $l_V$  is defined as the maximum range of the two-body interactions. For example,  $l_V = 1$  implies a range up to nearest-neighbor,  $l_V = 2$ , next nearest-neighbor, etc. The dashed black line shows the decay of the two-body interactions for  $\hat{H}_{WF}$  scaled by the average nearest-neighbor hopping. The other lines are the two-body interactions for the corresponding effective model with only a nearest-neighbor hopping term and a limited range two-body interaction. The error as defined in (4.14) is also shown in the last column of the legend.

body interaction? Given the previously outlined optimization procedure, the importance of these terms can be tested by fitting to Hamiltonians with increasingly longer-range single-body and two-body terms. The performance of each of these models can then be assessed relative to  $\hat{H}_{\text{WF}}$  by calculating,

$$\delta_e = \frac{E_{\min} - E_0^{WF}}{N_a} \quad (4.14)$$

where  $E_{\min}$  is the minimum value resulting from the minimization of (4.4) and  $E_0^{WF}$ , the ground state energy of  $\hat{H}_{\text{WF}}$  with  $N_a$  atoms. Small values of  $\delta_e$  are indicative of effective models which are more closely related to  $\hat{H}_{\text{WF}}$ .

In Fig. 4.8 we show the accuracy of different effective models when the range of the hopping and two-body interactions are constrained, but with the detailed shape of the interactions optimized subject to the constraint. For a pure Hubbard model,  $\delta_e = 3 \times 10^{-3}$ , in atomic units. If we increase only the hopping, the energy improves to  $1.7 \times 10^{-3}$  at a range of 3 lattice spacings. We get a much better improvement if we keep the hopping nearest-neighbor but increase the Coulomb repulsion out to a range of 3, with the energy error reducing by over an order of magnitude down to  $1.9 \times 10^{-4}$ . The best improvement comes from increasing both ranges, where we find an energy error well under  $10^{-4}$ . The optimal two-body terms smoothly decay to zero with distance as opposed to being sharply cut off. This decay is shown in Fig. 4.8(b) for several effective models with varying maximum interaction range. As the maximum range is increased, the two-body interactions smoothly approach those of the original model.

#### 4.4.4 Hubbard Model for the H-chain

The range of the one- and two-body interactions can be decreased even further so that the remaining terms in the effective model represent those of a pure Hubbard model, with only a

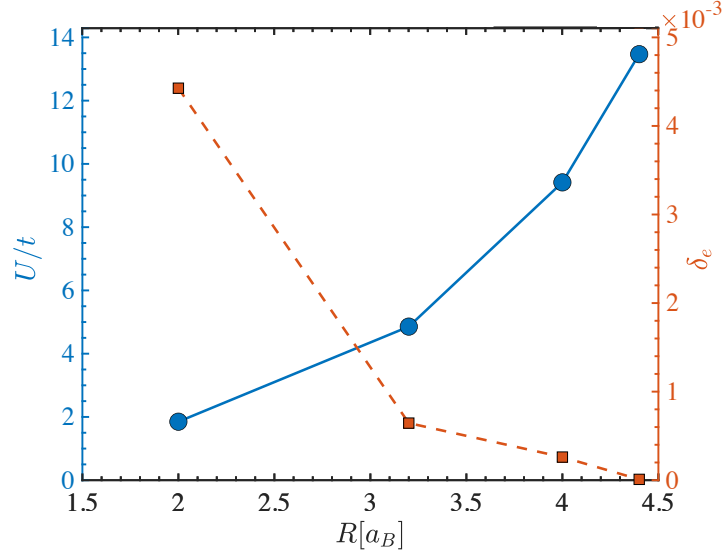


Figure 4.9: Optimal Hubbard parameters for each H-chain as a function of the atomic spacing,  $R$  for H100. The resulting Hubbard model becomes “strongly correlated” near  $R = 3 - 4a_B$  where the corresponding value of  $U/t$  becomes larger than the bandwidth of about  $4t$ . The dashed red line shows the optimization error as defined in Eq. (4.14).

nearest-neighbor hopping,  $t$ , an on-site interaction,  $U$  and a chemical potential  $\mu$ . We allow for slight variations of the model parameters near the edges so that the full Hamiltonian reads

$$\hat{H}_{\text{Hub}} = \sum_{\sigma, \langle ij \rangle} t_{ij}^{\text{H}} \hat{c}_{\sigma i}^{\dagger} \hat{c}_{\sigma j} + \sum_i U_i^{\text{H}} \hat{n}_{\uparrow i} \hat{n}_{\downarrow i} + \sum_i \mu_i^{\text{H}} \hat{n}_{\text{tot}, i} \quad (4.15)$$

For small  $R$ , the effective Hubbard model is expected to be in the weakly correlated regime, gradually becoming more and more correlated as  $R$  is increased. This behavior is shown in Fig. 4.9 for the optimal Hubbard models. We can see that beyond  $R = 3.2a_B$ , the effective model transitions into the strongly-correlated Hubbard regime where it is expected to be a better representation for the original H-chain. This can be seen in figures 4.5-4.7 which compare the spin velocities and correlations of the H-chains and their corresponding effective Hubbard models at  $R = 2.0a_B$  and  $R = 3.2a_B$ .

At  $R = 2.0a_B$ , the spin velocities for the 1- and 2-spinon pairs in the effective Hubbard



model show an error of  $\sim 6\%$  and  $\sim 8\%$  relative to the original H-chain, respectively. At larger  $R$ , these errors decrease to  $\sim 1\%$  for both excitations. Similarly, the decay of the single-particle Green's function can be measured as the slope of the lines shown in Fig. 4.6. For  $R = 2.0a_B$ , the decay rates between the effective Hubbard model and the H-chain differ by  $\sim 29\%$  whereas at larger  $R$ , the error decreases to  $\sim 16\%$ . This main difference lies within the decay of the tails as an on-site interaction alone can have difficulty in replicating the long-range correlations built up from having a similarly long-range interaction. Note that for  $\hat{H}_{\text{WF}}$ , the decay follows those of the original H-chain much closer in comparison. This is in contrast to the spin-spin correlations which show  $\hat{H}_{\text{Hub}}$  and  $\hat{H}_{\text{WF}}$  agreeing almost exactly as  $R$  increases from  $2.0a_B$  to  $3.2a_B$ .

The general good agreement between  $H_{\text{Hub}}$  and the original H-chain shows that in this case the long-range Coulomb interaction is not important in determining the ground state and spin excitations. However, it is important to remember that this system is at half-filling, and it is insulating. Doping the hydrogen chain is less natural than in a solid: one would need to add in an artificial neutralizing charge background. The long range Coulomb interaction is likely more important in the doped case. In addition, we have considered only large enough  $R$  so that diffuse bands are not occupied. The occupation of these outer bands self-dopes the 1S band and induces a metal-insulator transition[48]. In this case the long range Coulomb interaction may play an important role in both the interactions of the holes in the 1S band and in the physics of the diffuse electrons in the outer bands.

# Chapter 5

## Conclusion

The techniques presented in the previous chapters constitute an alternative downfolding scheme that includes reliable tests at each step of the process as well as useful comparisons to the traditional, DFT-based downfolding procedure. Focusing on the H-chain, we are able to determine the accuracy of various approximations by directly comparing them to simulations of the full system. Using sb-DMRG to construct “interacting Wannier functions” from a sum of single-particle density matrices, we found that the H-chain can be accurately represented by a simple effective model. Comparing the WFs formed by this approach to those obtained by Hartree-Fock, we see only slight differences, indicating that conventional DFT-based approaches are likely reliable in this regime. Despite their simplicity, these models are also able to capture the low-energy spin properties of the original system, such as spin velocities, single-particle correlations and spin-spin correlations. For more complicated materials, such comparisons may not be possible, but the approach described in section 4.3 remains valid, assuming the expectation value can be efficiently computed.

Using the variational optimization in section 4.3, the complicated two-particle interactions present in the WF transformed model can be renormalized to just a few terms, with the

range of the interactions controlling the resulting accuracy. The range can also be reduced to include only on-site interactions, allowing the H-chain to be represented by a pure Hubbard model without incurring too large an error. For a finite range, we find the optimized parameters smoothly decay to zero and tend not to contribute to an increasing entanglement in the insulating phase. The relationship between the range of the two body interaction and entanglement seems to be subtle and further investigation is required.

# Bibliography

- [1] O. Andersen, A. Liechtenstein, O. Jepsen, and F. Paulsen. Lda energy bands, low-energy hamiltonians,  $t'$ ,  $t''$ ,  $t_{\perp}(k)$ , and  $j_{\perp}$ . *Journal of Physics and Chemistry of Solids*, 56(12):1573–1591, 1995.
- [2] V. Anisimov and O. Gunnarsson. Density-functional calculation of effective coulomb interactions in metals. *Physical Review B*, 43(10):7570, 1991.
- [3] F. Aryasetiawan and O. Gunnarsson. The gw method. *Reports on Progress in Physics*, 61(3):237, 1998.
- [4] F. Aryasetiawan, M. Imada, A. Georges, G. Kotliar, S. Biermann, and A. Lichtenstein. Frequency-dependent local interactions and low-energy effective models from electronic structure calculations. *Physical Review B*, 70(19):195104, 2004.
- [5] A. D. Becke. A new mixing of hartree–fock and local density-functional theories. *The Journal of chemical physics*, 98(2):1372–1377, 1993.
- [6] V. Belinicher and A. Chernyshev. Consistent low-energy reduction of the three-band model for copper oxides with oo hopping to the effective t-j model. *Physical Review B*, 49(14):9746, 1994.
- [7] V. Belinicher, A. Chernyshev, and L. Popovich. Range of the t-j model parameters for cuo 2 planes: Experimental data constraints. *Physical Review B*, 50(18):13768, 1994.
- [8] V. Belinicher, A. Chernyshev, and V. Shubin. Generalized  $t-t'-j$  model: parameters and single-particle spectrum for electrons and holes in copper oxides. *Physical Review B*, 53(1):335, 1996.
- [9] V. Belinicher, A. Chernyshev, and V. Shubin. Single-hole dispersion relation for the real cu o 2 plane. *Physical Review B*, 54(21):14914, 1996.
- [10] S. Biermann, A. Poteryaev, A. Lichtenstein, and A. Georges. Dynamical singlets and correlation-assisted peierls transition in v o 2. *Physical review letters*, 94(2):026404, 2005.
- [11] G. K.-L. Chan, A. Keselman, N. Nakatani, Z. Li, and S. R. White. Matrix product operators, matrix product states, and ab initio density matrix renormalization group algorithms. *The Journal of chemical physics*, 145(1):014102, 2016.

- [12] H. J. Changlani, H. Zheng, and L. K. Wagner. Density-matrix based determination of low-energy model hamiltonians from ab initio wavefunctions. *The Journal of chemical physics*, 143(10):102814, 2015.
- [13] G. Cuono, C. Autieri, F. Forte, M. T. Mercaldo, A. Romano, A. Avella, and C. Noce. A minimal tight-binding model for the quasi-one-dimensional superconductor k2cr3as3. *New Journal of Physics*, 21(6):063027, 2019.
- [14] M. De Raychaudhury, E. Pavarini, and O. Andersen. Orbital fluctuations in the different phases of lavo 3 and yvo 3. *Physical review letters*, 99(12):126402, 2007.
- [15] J. Des Cloizeaux. Orthogonal orbitals and generalized wannier functions. *Physical Review*, 129(2):554, 1963.
- [16] J. Des Cloizeaux. Energy bands and projection operators in a crystal: Analytic and asymptotic properties. *Physical Review*, 135(3A):A685, 1964.
- [17] S. V. Faleev, M. Van Schilfgaarde, and T. Kotani. All-electron self-consistent g w approximation: Application to si, mno, and nio. *Physical review letters*, 93(12):126406, 2004.
- [18] M. Fishman, S. R. White, and E. M. Stoudenmire. The ITensor software library for tensor network calculations, 2020.
- [19] K. F. Freed. Is there a bridge between ab initio and semiempirical theories of valence? *Accounts of Chemical Research*, 16(4):137–144, 1983.
- [20] O. Gunnarsson. Calculation of parameters in model hamiltonians. *Physical Review B*, 41(1):514, 1990.
- [21] O. Gunnarsson, O. Andersen, O. Jepsen, and J. Zaanen. Density-functional calculation of the parameters in the anderson model: Application to mn in cdte. *Physical Review B*, 39(3):1708, 1989.
- [22] J. Hachmann, W. Cardoen, and G. K.-L. Chan. Multireference correlation in long molecules with the quadratic scaling density matrix renormalization group. *The Journal of chemical physics*, 125(14):144101, 2006.
- [23] L. Hedin. New method for calculating the one-particle green’s function with application to the electron-gas problem. *Physical Review*, 139(3A):A796, 1965.
- [24] P. Hohenberg and W. Kohn. Inhomogeneous electron gas. *Physical review*, 136(3B):B864, 1964.
- [25] M. S. Hybertsen, M. Schlüter, and N. E. Christensen. Calculation of coulomb-interaction parameters for la 2 cuo 4 using a constrained-density-functional approach. *Physical Review B*, 39(13):9028, 1989.

- [26] M. Imada and T. Miyake. Electronic structure calculation by first principles for strongly correlated electron systems. *Journal of the Physical Society of Japan*, 79(11):112001, 2010.
- [27] Y. Imai and M. Imada. Ground-state properties and optical conductivity of the transition metal oxide sr2vo4. *Journal of the Physical Society of Japan*, 75(9):094713, 2006.
- [28] Y. Imai, I. Solovyev, and M. Imada. Electronic structure of strongly correlated systems emerging from combining path-integral renormalization group with the density-functional approach. *Physical review letters*, 95(17):176405, 2005.
- [29] R. O. Jones and O. Gunnarsson. The density functional formalism, its applications and prospects. *Reviews of Modern Physics*, 61(3):689, 1989.
- [30] E. Koch and S. Goedecker. Locality properties and wannier functions for interacting systems. *Solid State Communications*, 119(2):105–109, 2001.
- [31] W. Kohn. Analytic properties of bloch waves and wannier functions. *Physical Review*, 115(4):809, 1959.
- [32] W. Kohn and L. J. Sham. Self-consistent equations including exchange and correlation effects. *Physical review*, 140(4A):A1133, 1965.
- [33] T. Kotani, M. Van Schilfgaarde, and S. V. Faleev. Quasiparticle self-consistent gw method: A basis for the independent-particle approximation. *Physical Review B*, 76(16):165106, 2007.
- [34] W. Kutzelnigg. Generalized k-particle brillouin conditions and their use for the construction of correlated electronic wavefunctions. *Chemical Physics Letters*, 64(2):383–387, 1979.
- [35] C. Lee, W. Yang, and R. G. Parr. Development of the colle-salvetti correlation-energy formula into a functional of the electron density. *Physical review B*, 37(2):785, 1988.
- [36] T. Leung, X. Wang, and B. Harmon. Band-theoretical study of magnetism in sc 2 cuo 4. *Physical Review B*, 37(1):384, 1988.
- [37] M. Levy. Universal variational functionals of electron densities, first-order density matrices, and natural spin-orbitals and solution of the v-representability problem. *Proceedings of the National Academy of Sciences*, 76(12):6062–6065, 1979.
- [38] A. Liebsch. Surface versus bulk coulomb correlations in photoemission spectra of s r v o 3 and c a v o 3. *Physical review letters*, 90(9):096401, 2003.
- [39] N. Lin, C. Marianetti, A. J. Millis, and D. R. Reichman. Dynamical mean-field theory for quantum chemistry. *Physical review letters*, 106(9):096402, 2011.
- [40] P.-O. Löwdin. On the non-orthogonality problem connected with the use of atomic wave functions in the theory of molecules and crystals. *The Journal of Chemical Physics*, 18(3):365–375, 1950.

- [41] P.-O. Löwdin. A note on the quantum-mechanical perturbation theory. *The Journal of Chemical Physics*, 19(11):1396–1401, 1951.
- [42] P.-O. Löwdin. Studies in perturbation theory: Part vi. contraction of secular equations. *Journal of Molecular Spectroscopy*, 14(1-4):112–118, 1964.
- [43] N. Marzari, A. A. Mostofi, J. R. Yates, I. Souza, and D. Vanderbilt. Maximally localized wannier functions: Theory and applications. *Reviews of Modern Physics*, 84(4):1419, 2012.
- [44] N. Marzari and D. Vanderbilt. Maximally localized generalized wannier functions for composite energy bands. *Physical review B*, 56(20):12847, 1997.
- [45] L. Mattheiss. Electronic band properties and superconductivity in  $\text{La}_2\text{CuO}_4$ . *Physical review letters*, 58(10):1028, 1987.
- [46] T. Miyake, K. Nakamura, R. Arita, and M. Imada. Comparison of ab initio low-energy models for  $\text{LaFePO}_4$ ,  $\text{LaFeAsO}$ ,  $\text{BaFe}_2\text{As}_2$ ,  $\text{LiFeAs}$ ,  $\text{FeSe}$ , and  $\text{FeTe}$ : electron correlation and covalency. *Journal of the Physical Society of Japan*, 79(4):044705, 2010.
- [47] M. Motta, D. M. Ceperley, G. K.-L. Chan, J. A. Gomez, E. Gull, S. Guo, C. A. Jiménez-Hoyos, T. N. Lan, J. Li, F. Ma, et al. Towards the solution of the many-electron problem in real materials: Equation of state of the hydrogen chain with state-of-the-art many-body methods. *Physical Review X*, 7(3):031059, 2017.
- [48] M. Motta, C. Genovese, F. Ma, Z.-H. Cui, R. Sawaya, G. K.-L. Chan, N. Chepiga, P. Helms, C. Jiménez-Hoyos, A. J. Millis, et al. Ground-state properties of the hydrogen chain: Dimerization, insulator-to-metal transition, and magnetic phases. *Physical Review X*, 10(3):031058, 2020.
- [49] K. Nakamura, R. Arita, and M. Imada. Ab initio derivation of low-energy model for iron-based superconductors  $\text{LaFeAsO}$  and  $\text{LaFePO}_4$ . *Journal of the Physical Society of Japan*, 77(9):093711, 2008.
- [50] K. Nakamura, Y. Yoshimoto, T. Kosugi, R. Arita, and M. Imada. Ab initio derivation of low-energy model for  $\kappa$ -et type organic conductors. *Journal of the Physical Society of Japan*, 78(8):083710–083710, 2009.
- [51] Y. Otsuka and M. Imada. First-principles computation of  $\text{YVO}_3$ : Combining path-integral renormalization group with density-functional approach. *Journal of the Physical Society of Japan*, 75(12):124707, 2006.
- [52] D. E. Parker, X. Cao, and M. P. Zaletel. Local matrix product operators: Canonical form, compression, and control theory. *Physical Review B*, 102(3):035147, 2020.
- [53] E. Pavarini, S. Biermann, A. Poteryaev, A. Lichtenstein, A. Georges, and O. Andersen. Mott transition and suppression of orbital fluctuations in orthorhombic  $\text{3d1}$  perovskites. *Physical review letters*, 92(17):176403, 2004.

- [54] J. P. Perdew, K. Burke, and M. Ernzerhof. Generalized gradient approximation made simple. *Physical review letters*, 77(18):3865, 1996.
- [55] W. H. Press, W. T. Vetterling, S. A. Teukolsky, and B. P. Flannery. *Numerical recipes in C++ the art of scientific computing*. Cambridge university press, 2001.
- [56] M. Schüler, M. Rösner, T. Wehling, A. Lichtenstein, and M. Katsnelson. Optimal hubbard models for materials with nonlocal coulomb interactions: graphene, silicene, and benzene. *Physical Review Letters*, 111(3):036601, 2013.
- [57] K. V. Shanavas and S. Satpathy. Effective tight-binding model for  $m \times 2$  under electric and magnetic fields. *Physical Review B*, 91(23):235145, 2015.
- [58] H. Shinaoka, M. Troyer, and P. Werner. Accuracy of downfolding based on the constrained random-phase approximation. *Physical Review B*, 91(24):245156, 2015.
- [59] A. V. Sinitskiy, L. Greenman, and D. A. Mazziotti. Strong correlation in hydrogen chains and lattices using the variational two-electron reduced density matrix method. *The Journal of chemical physics*, 133(1):014104, 2010.
- [60] I. Solovyev. Combining dft and many-body methods to understand correlated materials. *Journal of Physics: Condensed Matter*, 20(29):293201, 2008.
- [61] I. Solovyev and M. Imada. Screening of coulomb interactions in transition metals. *Physical Review B*, 71(4):045103, 2005.
- [62] P. J. Stephens, F. J. Devlin, C. F. Chabalowski, and M. J. Frisch. Ab initio calculation of vibrational absorption and circular dichroism spectra using density functional force fields. *The Journal of physical chemistry*, 98(45):11623–11627, 1994.
- [63] P. Sterne and C. Wang. Oxygen vacancies and antiferromagnetism in  $\text{La}_2\text{CuO}_4$ . *Physical Review B*, 37(13):7472, 1988.
- [64] E. M. Stoudenmire and S. R. White. Sliced basis density matrix renormalization group for electronic structure. *Physical review letters*, 119(4):046401, 2017.
- [65] S. Ten-no. Stochastic determination of effective hamiltonian for the full configuration interaction solution of quasi-degenerate electronic states. *The Journal of chemical physics*, 138(16):164126, 2013.
- [66] T. Tsuchimochi and G. E. Scuseria. Strong correlations via constrained-pairing mean-field theory, 2009.
- [67] M. van Schilfgaarde, T. Kotani, and S. Faleev. Quasiparticle self-consistent g w theory. *Physical review letters*, 96(22):226402, 2006.
- [68] S. H. Vosko, L. Wilk, and M. Nusair. Accurate spin-dependent electron liquid correlation energies for local spin density calculations: a critical analysis. *Canadian Journal of physics*, 58(8):1200–1211, 1980.



- [69] G. H. Wannier. The structure of electronic excitation levels in insulating crystals. *Physical Review*, 52(3):191, 1937.
- [70] S. R. White. Numerical canonical transformation approach to quantum many-body problems. *The Journal of chemical physics*, 117(16):7472–7482, 2002.
- [71] T. Yanai and G. K.-L. Chan. Canonical transformation theory for multireference problems. *The Journal of chemical physics*, 124(19):194106, 2006.
- [72] J. Zaanen, O. Jepsen, O. Gunnarsson, A. Paxton, O. Andersen, and A. Svane. What can be learned about hightc from local density theory? *Physica C: Superconductivity*, 153:1636–1641, 1988.
- [73] H. Zheng, H. J. Changlani, K. T. Williams, B. Busemeyer, and L. K. Wagner. From real materials to model hamiltonians with density matrix downfolding. *Frontiers in Physics*, 6:43, 2018.

# Appendix A

## Appendix

### A.1 Code Usage

The routines presented in the github repo are used to determine a set of effective Hamiltonian model parameters from another set of parameters representing the full system. The code is written as a mixture of Julia and C++ programs where a short Julia script is used to setup the main calculation which is later done in the C++ ITensor library[18]. Note that there is now a Julia version of the ITensor library(<https://github.com/ITensor/ITensors.jl>), which can be used to streamline the overall process.

#### A.1.1 Setting up a Calculation

The first step is to define the structure of the new Hamiltonian and initialize it with values from the original system. This will decide things such as the extent of the hopping terms(nearest-neighbor, next nearest-neighbor, etc.) and the range of the two-body interactions. We begin with `PrepEffH.jl` which produces a set of output files that can then be fed

into EffHubbardBFGS.

## PrepEffH.jl

A list of all the inputs and descriptions can be seen by calling `julia PrepEffH.jl --help`.

For convenience we list these here

```
usage: PrepEffH.jl [-o O] [--sym] [--cap_edge CAP_EDGE] [-h] N fn_tij
                fn_Vij N_terms_tij N_terms_Vij
```

positional arguments:

N	System size(number of atoms)
fn_tij	File containing the single-particle terms for the full Hamiltonian in the form [...; i j tij; i (j+1) ti(j+1); ...]
fn_Vij	File containing the two-particle terms for the full Hamiltonian in the form [...; i j Vij; i (j+1) Vi(j+1); ...]
N_terms_tij	Number of variational terms in tij(including onsite term) (type: Int64)
N_terms_Vij	Number of variational terms in Vij(including onsite term) (type: Int64)

optional arguments:

-o O	Directory into which to output results (default: ".")
--sym	Flag, when called, symmetrized tij and Vij

```

                                about the center of the 1D chain
--cap_edge CAP_EDGE  Bounds the maximum edge region to cap_edge
                        (type: Int64, default: 10000)
-h, --help           show this help message and exit

```

The `N_terms_tij` and `N_terms_Vij` require some more clarification. These are essentially the range of the one- and two-particle interactions, respectively. For example, setting `N_terms_tij` to 2 will generate two variational parameters for the single-particle terms, one that acts as a chemical potential the other acting as a nearest-neighbor hopping

$$t_{ij} = \begin{cases} \mu & i = j \\ t & |i - j| = 1 \\ 0 & \text{otherwise} \end{cases} \quad (\text{A.1})$$

The same is done for the two-particle terms defined by `N_terms_Vij`. This is a consequence of the translational invariance of the 1D system.

The code then creates a directory named `EffH*` (name varies depending on the input values) which is saved to the path specified by the `-o` flag and outputs several files listed below

```
tij_eff.txt
```

The initialized one-particle terms of the new model in a three-column format

```
[i j tij]
```

```
Vij_eff.txt
```

The initialized two-particle terms of the new model in a three-column format

```
[i j Vij]
```

`tij_full.txt`

The original one-particle terms in a three-column format `[i j tij]`

`Vij_full.txt`

The original two-particle terms in a three-column format `[i j Vij]`

`tijvar.txt`

The variable IDs(1 for the first variational parameter, 2 for the second variational parameter, etc.) for the one-particle terms in a three-column format `[i j <variable ID>]`

`Vijvar.txt`

The variable IDs(1 for the first variational parameter, 2 for the second variational parameter, etc.) for the two-particle terms in a three-column format `[i j <variable ID>]`

**Walking through the Code** The main function is called `main` and begins with importing the one- and two-particle terms from the provided file names, calling a helper function `to_mat` which converts these into  $N \times N$  matrices, `tij` and `Vij` in the code. Next, the variable matrices, `tij_var_mat` and `Vij_var_mat`, are created using the function `get_var_mats` which define the structure of the model Hamiltonian. The routine takes into account any differences the user wants to include near the edges(specified by `--cap_edge`) and produces

matrices which take the form

$$V = \begin{pmatrix} v_1 & v_4 & v_6 & 0 & \cdots & 0 & 0 & 0 & 0 \\ v_4 & v_2 & v_5 & v_6 & \cdots & 0 & 0 & 0 & 0 \\ v_6 & v_5 & v_3 & v_5 & \cdots & 0 & 0 & 0 & 0 \\ 0 & v_6 & v_5 & v_3 & \cdots & 0 & 0 & 0 & 0 \\ \vdots & \vdots & \vdots & \vdots & \ddots & \vdots & \vdots & \vdots & \vdots \\ 0 & 0 & 0 & 0 & \cdots & v_3 & v_5 & v_6 & 0 \\ 0 & 0 & 0 & 0 & \cdots & v_5 & v_3 & v_5 & v_6 \\ 0 & 0 & 0 & 0 & \cdots & v_6 & v_5 & v_2 & v_4 \\ 0 & 0 & 0 & 0 & \cdots & 0 & v_6 & v_4 & v_1 \end{pmatrix} \quad (\text{A.2})$$

for  $N\_terms\_Vij = 3$ . In the example above, the main diagonal contains two sites near the edge which are allowed to break translational invariance as well as one site for the  $|i - j| = 1$  terms. In this case, the edge regions are defined by the procedure outlined in section 4.3 for a large system size of 100 atoms. The classification of “edge” versus “bulk” for this system is shown in Fig. A.1. However, if the same is done for the one-particle terms, the procedure fails.

As shown in the blue curve in Fig. A.1(b), the “edge” region determined by using the previous method for the  $0^{th}$  diagonal of  $t_{ij}$  is quite large and therefore ill-defined. This can be traced back to the incorporation of the electron-lattice interaction terms from the original hydrogen chain into the lattice model.

The original hydrogen chain accounts for the electron-lattice interaction by adding an on-site potential of the form

$$U_n = \sum_{n'} V_{nn'} \quad (\text{A.3})$$

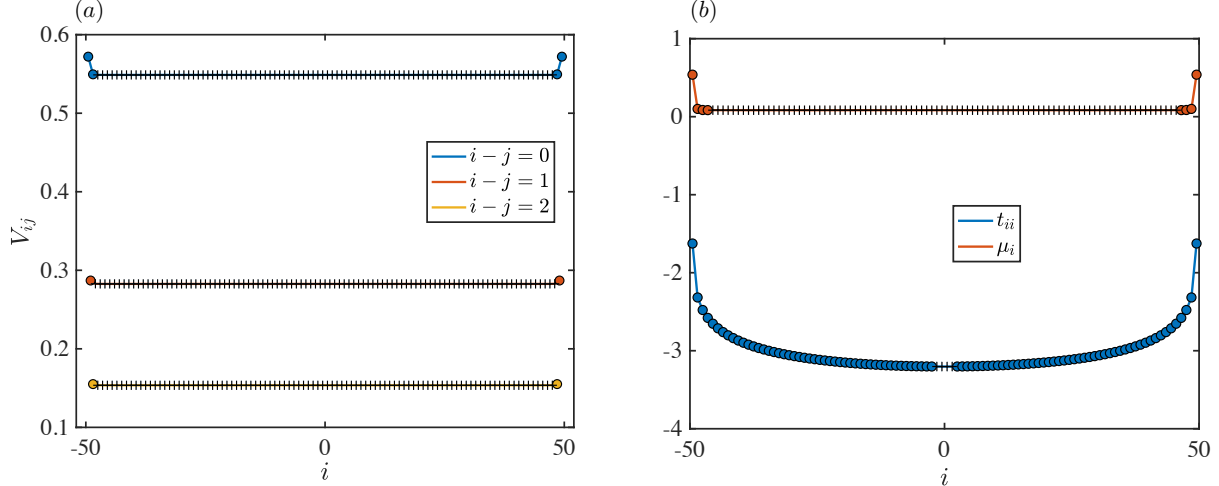


Figure A.1: (a) The edge regions for the two-particle interactions defined by the procedure in section 4.3. The colored circles denote “edges” and the black crosses, the “bulk”. (b) The edge regions for the one-particle terms defined in the same scheme for the original values of the on-site terms in blue and the new terms calculated as a chemical potential by measuring the density-density interactions with respect to half-filling in red. Note that in the latter, the edge regions are much more well defined.

where  $n$  and  $n'$  enumerate the slices. After transforming to the lattice representation using the Wannier functions, this term gets integrated into the diagonal of  $t_{ij}$  (among other terms, but less so due to the highly localized nature of the Wannier functions), which couples the values of the interactions with those of the single-particle terms. The Wannier functions mix the two in a complicated way, but we can guess that the electron-lattice interaction of the lattice model takes on a similar form to that of the hydrogen chain. From this perspective, we can express  $\hat{H}_{full}$  as,

$$\hat{H}_{WF} = \sum_{i \neq j} t_{ij} \hat{c}_{\sigma i}^\dagger \hat{c}_{\sigma j} + \frac{1}{2} \sum_{ij} V_{ij} \hat{n}_i \hat{n}_j + \sum_i \left( \mu_i - \sum_j V_{ij} \right) \hat{n}_i \quad (\text{A.4})$$

where  $\mu_i \equiv t_{ii} + \sum_j V_{ij}$ . This is nothing more than writing a Hamiltonian with the density-density interactions measured with respect to half-filling.

At first, this seems like a trivial modification, but after calculating  $\mu_i$  at different system sizes, we can see that it behaves as a positive chemical potential with a clearly defined “bulk”

and “edge” region(see Fig. A.1(b)). Together with the “bulk” and “edge” regions defined for  $\tilde{t}_{ij}$  and  $\tilde{V}_{ij}$ ,  $\hat{H}_{eff}$  can now be expressed in terms of a small number of well regularized variational parameters as,

$$\hat{H}_{eff} = \sum_{i \neq j} \tilde{t}_{ij} \hat{c}_{\sigma i}^\dagger \hat{c}_{\sigma j} + \frac{1}{2} \sum_{ij} \tilde{V}_{ij} \hat{n}_i \hat{n}_j + \sum_i \left( \tilde{\mu}_i - \sum_j \tilde{V}_{ij} \right) \hat{n}_i \quad (\text{A.5})$$

In the code, this is taken into account by adjusting the diagonal elements of the effective one-particle terms. Once the variables are defined, all the output files are written to disc. The next step is to call `EffHubbardBFGS` within the newly created directory to run the optimization.

## EffHubbardBFGS

After using `PrepEffH.jl` to create the directory `EffH*`, we can call `EffHubbardBFGS` in that same directory to begin running the optimization. The optimization is carried out with the help of the ITensor library and a minimization routine taken from [55]. In the current framework, we choose the Broyden-Fletcher-Goldfarb-Shanno(BFGS) algorithm to minimize 4.4 and find the effective model parameters. The BFGS routine is written in `BFGS.h`. The main inputs are pointers to functions which can evaluate 4.4 and it’s derivatives called `*func` and `*dfunc` in the code. The functions themselves are written as sub-routines in `EffHubbardBFGS` called `dmrg_func` and `ddmrg_func`.

**Walking through the Code** The program begins by first reading in the files generated by `PrepEffH.jl`. It then constructs and stores the full Hamiltonian as an MPO which will later be used by `dmrg_func` and `ddmrg_func` to evaluate the optimization function. An initial Néel state wavefunction is then used as a starting point for the first DMRG calculation on the effective model giving  $|\Psi_{eff}\rangle_0$ . At this stage, we have all the ingredients to begin the



optimization and call the BFGS routine.

Each step of BFGS will call `dmrg_func` and `ddmrg_func` a certain number of times depending on the results of the line search algorithm. Each call requires a specific number of DMRG sweeps which can be controlled by modifying these functions. Currently, the code is configured to run one sweep for each call to `dmrg_func` and  $2N_{\text{var}}$  sweeps for each call to `ddmrg_func`, where  $N_{\text{var}}$  is the number of variables.

After the optimization has converged, the number of iterations and function calls are printed to the screen as well as saved to disc. The newly found model parameters are stored in the files `BFGS_newtij_eff.txt` and `BFGS_newVij_eff.txt` in the three-column format described in the previous section.

## **AltOptimize.jl**

Optimizing both the one- and two-particle terms at the same time can cause the procedure to become stuck in local minima. We can mitigate this effect by minimizing the terms separately, first minimizing with respect to the one-particle terms, then fix these for an optimization of the two-particle terms, and repeating in this fashion until the minimization converges. This is the purpose of `AltOptimize.jl`. It is a short Julia script that calls `EffHubbardBFGS` in the sequential manner just described and keeps track of the terms at each step, saving the output of `EffHubbardBFGS` after each call. After running `PrepEffH.jl`, we can run `AltOptimize.jl` in the `EffH*` directory to begin this alternating optimization.